Acta Pharmaceutica Sinica B 2026;16(3):1530−1549

Chinese Pharmaceutical Association
Institute of Materia Medica, Chinese Academy of Medical Sciences

Acta Pharmaceutica Sinica B

www.elsevier.com/locate/apsb
www.sciencedirect.com

ORIGINAL ARTICLE

Mechanistic insights into ligand selectivity in μ- and δ-opioid receptors beyond the "message−address" conceptual framework

Xin Zhang[a,†], Hongyan Song[a,†], Ruofan Chen[a,†], Xinran Kong[a,†], Jin Wang[a,*], Xinghua Li[a,*], Ye Yu[a,b,*]

[a]*Schools of Basic Medicine and Clinical Pharmacy and Traditional Chinese Pharmacy, and State Key Laboratory of Natural Medicines, China Pharmaceutical University, Nanjing 211198, China*
[b]*Key Laboratory of Preclinical Study for New Drugs of Gansu Province, School of Basic Medical Sciences, Lanzhou University, Lanzhou 730000, China*

Received 14 April 2025; received in revised form 12 August 2025; accepted 5 September 2025

KEY WORDS

Opioid receptor;
Neuropharmacology;
Binding pathway;
Message−address concept;
Analgesia;
Receptor selectivity;
Endomorphin-1;
Morphine

Abstract Ligand selectivity between μ-opioid receptors (μ-OR) and δ-opioid receptors (δ-OR) is key for improving opioid analgesics. While the "message−address" hypothesis has been central to explaining this selectivity, we present evidence for an additional mechanism. Chimeric receptor and mutagenesis studies identify residue 2.63 in the orthosteric pocket as a key determinant of morphine's μ/δ-OR selectivity, while EM-1's selectivity involves a combination of residues at positions 2.63 and 3.29, the N-terminus, and extracellular loop 3 (ECL3). Approaches like voltage-clamp fluorometry, engineered zinc-bridge and microscale thermophoresis show that EM-1's $Y^1P^2W^3F^4$ sequence confers over 1500-fold μ/δ-OR selectivity, driven by steric hindrance and a β-turn structure. β-Endorphin, with a more flexible sequence, binds non-selectively to both receptors. Morphine's rigid isoquinoline scaffold and broader geometry restrict it to binding through the wide ECL2-transmembrane (TM) 5 cleft, explaining its modest μ/δ-OR selectivity. These findings reveal that μ/δ-OR selectivity is driven by both "message−address" interactions and receptor−specific binding pathways, advancing opioid drug design.

*Corresponding authors.
E-mail addresses: wangjin@cpu.edu.cn (Jin Wang), lixh@cpu.edu.cn (Xinghua Li), yuye@cpu.edu.cn (Ye Yu).
[†]These authors made equal contributions to this work.
Peer review under the responsibility of Chinese Pharmaceutical Association and Institute of Materia Medica, Chinese Academy of Medical Sciences.

https://doi.org/10.1016/j.apsb.2025.11.039

1. Introduction

The G protein-coupled receptor (GPCR) family represents the largest and most diverse group of membrane protein receptors and is a cornerstone of modern drug development[1]. Opioid receptors (ORs), members of the Class A GPCRs, are primarily categorized into μ-opioid receptors (μ-OR), δ-opioid receptors (δ-OR), and κ-opioid receptors (κ-OR), with μ-OR serving as the principal target for highly effective clinical analgesics[2]. However, μ-OR activation is often accompanied by significant side effects, including addiction, tolerance, respiratory depression, and constipation, limiting their therapeutic utility[2,3]. Overcoming these limitations necessitates the design of functionally selective ligands that harness distinct structural features of opioid receptors. Such ligands—including bivalent[4,5] and biased[6-8] ligands—hold the potential to minimize adverse effects[9,10], thereby paving the way toward the development of safer and more efficacious analgesics[11]. Endogenous ligands also demonstrate diverse selectivity profiles[12], such as the non-selective μ-OR/δ-OR peptide β-endorphin[13] and the μ-OR-specific tetrapeptides endomorphin-1 (EM-1, $Y^1P^2W^3F^4$-NH_2) and endomorphin-2 (EM-2, $Y^1P^2F^3F^4$-NH_2)[14]. Yet, the evolutionary mechanisms driving receptor subtype selectivity remain elusive. Unraveling these mechanisms is crucial not only for optimizing opioid drug development but also for deepening our understanding of how endogenous ligands evolved to achieve selective receptor interactions.

Class A GPCRs are characterized by a conserved orthosteric binding pocket[15], formed by seven transmembrane helices, which creates a large cavity subdivided into multiple functional subpockets[16]. This pocket is partially shielded by three extracellular loops (ECL1, ECL2, and ECL3) and the N-terminal domain, imparting a semi-buried architecture[17]. Investigations into the interactions of endogenous peptides and exogenous small molecules with three main types of opioid receptors—μ-OR, δ-OR, and κ-OR—have revealed nuanced mechanisms of ligand selectivity and binding affinity[18-20]. The "message−address" hypothesis, introduced in the 1970s, has been pivotal in rationalizing these interactions[21,22]. This model proposes that ligands are composed of a "message" motif, responsible for receptor binding and activation, and an "address" segment, which enhances the binding affinity and receptor subtype specificity[21] (Fig. 1A). This conceptual framework has driven the design of highly selective opioid receptor agonists and antagonists for decades[22-24]. Insights from structural studies have pinpointed key conserved residues[25,26]—$D^{3.32}$, $H^{6.52}$, and $Y^{7.43}$ (Ballesteros/Weinstein numbering[27])—as crucial mediators of the "message" function. In contrast, the "address" region is shaped by non-conserved residues in the upper portion of the orthosteric pocket. For example, δ-OR-selective antagonists like naltrindole[18] depend on interactions with $L^{7.35}$ and $W^{6.58}$, whereas κ-OR ligands such as nor-BNI and GNTI exploit $E^{6.58}$ for selectivity[19]. Longer peptide ligands extend their interactions beyond the orthosteric pocket, engaging non-conserved extracellular residues to achieve specificity. The δ-OR endogenous peptide deltorphin, for instance, interacts with ECL3, $W^{6.58}$, and $K^{2.63}$, achieving more than 1000-fold selectivity for δ-OR[20]. These findings underscore the complementary roles of conserved and non-conserved residues in opioid receptor selectivity, providing a framework for designing receptor-specific opioid therapeutics.

The "message−address" hypothesis, however, fails to fully account for the selectivity observed in all opioid receptor ligands[19,28]. For example, β-endorphin, despite its extended 27-residue "address" domain, shows no discernible preference between μ-OR and δ-OR[29,30] (Fig. 1B). In contrast, the endogenous tetrapeptides EM-1 and EM-2 achieve remarkable μ-OR selectivity (>1500-fold over δ-OR) without any apparent "address" sequence[31] (Fig. 1B). Unlike β-endorphin, EM-1 and EM-2 lack the extended peptide length necessary for direct interactions with ECL1, ECL3, or the N-terminal domain, as confirmed by the structure of the EM-1/human μ-OR (hμ-OR) complex (PDB ID: 8F7R)[20]. Similarly, the human κ-OR(hκ-OR)/JDTic complex (PDB ID: 4DJH)[19] reveals that JDTic and its derivatives achieve more than 1000-fold selectivity for hκ-OR without engaging in "address" interactions with $E^{6.58}$. These observations challenge the sufficiency of non-conserved orthosteric pocket residues as the sole drivers of selectivity, suggesting the need to refine the "message−address" hypothesis or explore alternative models. Additionally, structural studies of the BU72/mouse μ-OR (mμ-OR) complex (PDB ID: 5C1M)[32] provide compelling evidence that ECL1-3 and the N-terminal domain encapsulate the μ-OR orthosteric pocket, creating a partially buried ligand-binding site (Fig. 1C). The EM-1/hμ-OR structure (PDB ID: 8F7R) also reveals a substantial gap between the pocket's entry point and the activation site at its base[20]. This raises intriguing questions about how key residues in ligands like EM-1 ($Y^1P^2W^3F^4$) and β-endorphin ($Y^1G^2G^3F^4$) navigate these binding pathways and whether such differences contribute to their contrasting μ-OR/δ-OR selectivity profiles. Morphine, one of the most widely used opioids for over two centuries[33], exhibits modest selectivity (20-fold) for μ-OR over δ-OR, despite its structural divergence from both EM-1 and β-endorphin. Elucidating the mechanisms underlying morphine's limited μ-/δ-OR selectivity remains an important avenue for further studies.

To elucidate the molecular basis of opioid receptor subtype selectivity, we engineered μ-OR/δ-OR chimeric receptors and performed gain-of-function mutagenesis, identifying critical amino acid residues that govern EM-1 and morphine selectivity. EM-1 exhibits precise μ-OR versus δ-OR discrimination by interacting with residues at positions 2.63 and 3.29 and forming additional coupling with ECL3 and the N-terminal domain. In contrast, morphine's weak μ-OR/δ-OR selectivity is mediated through its interactions with residues at positions 2.63 and 7.35. Intriguingly, modifying the side-chain size of amino acids within ECL1 and the N-terminal region enables β-endorphin, an endogenous peptide typically lacking receptor selectivity, to "acquire" preferential binding to either μ-OR or δ-OR. Through enhanced conformational sampling, engineered zinc bridge, and incorporation of the fluorescent unnatural amino acid (flUAA) Anap, combined with voltage-clamp fluorometry (VCF) to monitor protein conformational dynamics, we identified distinct ligand entry pathways. EM-1 accesses the orthosteric pocket through a narrow cleft formed by ECL3 and the N-terminal domain, whereas morphine utilizes a broader pathway at the ECL2−TM5 interface. The bulky side chains and β-turn structure of EM-1 ($Y^1P^2W^3F^4$) impede its δ-OR binding by limiting accessibility and reducing affinity. Conversely, β-endorphin, with smaller and more flexible side chains ($Y^1G^2G^3F^4$), exhibits comparable accessibility to both μ-OR and δ-OR, resulting in non-selectivity. By elucidating the mechanisms of μ-OR/δ-OR selectivity, this study refines and extends the "message−address" hypothesis, providing insights into the evolutionary divergence of endogenous peptides and their selectivity profiles.

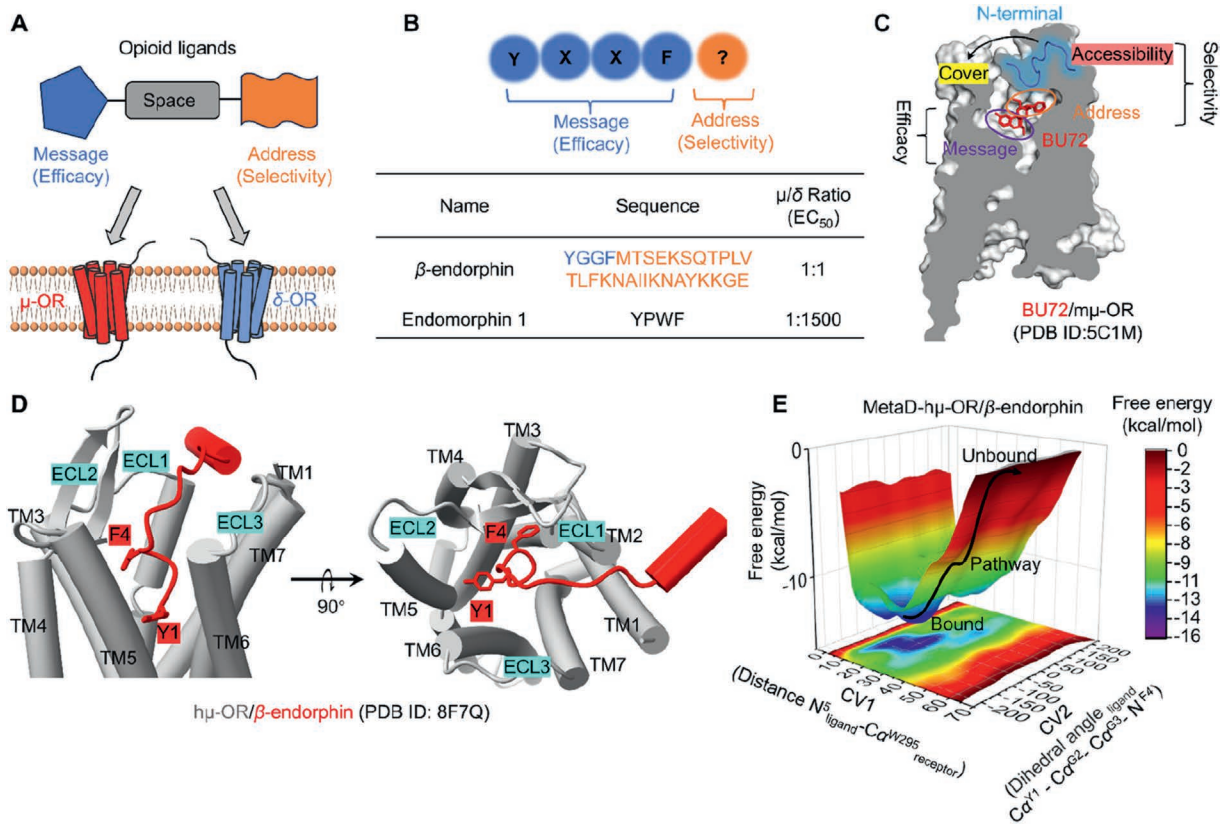

Figure 1 The "message−address" conceptual framework and the binding mechanism of β-endorphin's $Y^1G^2G^3F^4$ motif at the hμ-OR orthosteric site *via* the extracellular loop (ECL)1-ECL3 cleft. (A) Conceptual diagram of the "message−address" model for opioid receptor ligands. The "message" structure (blue) mediates receptor activation, whereas the "address" structure (orange) enhances receptor selectivity and binding affinity. (B) Application of the "message−address" hypothesis to opioid peptides. The conserved YXXF sequence functions as the "message" motif responsible for activation, while adjacent peptide regions serve as "address" structures, providing selectivity and affinity. (C) Sectional rendering of BU72 (red, stick representation) bound to the mμ-OR orthosteric pocket (PDB ID: 5C1M, gray). The "message" domain (solid purple circle) anchors to the basal orthosteric pocket, while the "address" domain (solid orange circle) occupies an upper sub-pocket. The receptor's N-terminal domain (blue) partially encapsulates the binding site, forming a protective cover. (D) β-endorphin binding to hμ-OR (PDB ID: 87FQ). The N-terminal $Y^1G^2G^3F^4$ sequence tightly engages the orthosteric pocket, while the C-terminal domain extends outward, threading through the cleft formed by ECL1 and ECL3. Side and top views (left and right, respectively) depict β-endorphin's orientation in the receptor pocket. The cleft between ECL1 and ECL3 serves as the entry site for the $Y^1G^2G^3F^4$ motif. (E) Metadynamics (MetaD) simulations reveal the free energy landscape of β-endorphin binding to hμ-OR, providing insight into conformational sampling during ligand binding. The black wavy line highlights the energy changes associated with intermediate binding states, supporting the proposed binding mechanism.

2. Results

2.1. Engineering selective binding of β-endorphin to μ-/δ-ORs via N-terminal and extracellular loop (ECL) modifications

Cryo-electron microscopy (cryo-EM) structural analysis[34,35] of the hμ-OR/β-endorphin complex (PDB ID: 8F7Q)[36] reveals that β-endorphin's "message" motif ($Y^1G^2G^3F^4$) is tightly bound within the orthosteric pocket of hμ-OR, with its C-terminal region extending extracellularly between ECL1 and ECL3 (Fig. 1D). This finding suggests that the $Y^1G^2G^3F^4$ core accesses the orthosteric pocket *via* a defined pathway, while the remaining 27 amino acids, forming secondary structural elements, primarily stabilize the $Y^1G^2G^3F^4$−hμ-OR interaction rather than conferring μ-/δ-OR selectivity, consistent with β-endorphin's non-selective binding profile. To investigate the pathway by which $Y^1G^2G^3F^4$ reaches the hμ-OR orthosteric pocket and to identify potential entry routes for other ligands such as EM-1 and morphine, we supplemented the structural information of the hμ-OR/β-endorphin complex (PDB ID: 8F7Q) with N-terminal data from the BU72/mμ-OR structure (PDB ID: 5C1M). Using metadynamics (MetaD) simulations[37], we enhanced conformational sampling to explore the dynamic interactions of the $Y^1G^2G^3F^4$ motif along its path to the orthosteric pocket, under the assumption that binding and dissociation pathways are analogous[38]. Two collective variables (CVs) were defined (Fig. 1E). CV1, the interatomic distance between the Cα atom of $W295^{6.48}$ and the nitrogen atom of the Y1 residue in β-endorphin, was chosen based on the well-documented role of $W295^{6.48}$ as a structurally conserved anchor at the base of the orthosteric binding pocket, where it forms persistent interactions with β-endorphin during receptor activation. CV2 was defined as the dihedral angle involving four consecutive backbone atoms—C_α^{Y1}, C_α^{G2}, C_α^{G3} and N^{F4}—to enable thorough sampling of the ligand's torsional flexibility, thereby capturing a broad range of plausible binding conformations (Fig. 1E). The reconstructed free energy landscape (Fig. 1E) revealed a pathway

for $Y^1G^2G^3F^4$ traversing the cleft between ECL1 and ECL3 to access (or exit) the orthosteric pocket (Supporting Information Fig. S1A). This process is characterized by a series of specific interactions: initially, the $Y^1G^2G^3F^4$ motif engaged with the N-terminal region of hμ-OR, forming hydrogen bonds with polar residues $L52^{N\text{-terminal}}$ and $D56^{N\text{-terminal}}$ (Fig. S1B). As the motif progressed, it disengaged from $L52^{N\text{-terminal}}$ but retains interaction with $D56^{N\text{-terminal}}$ (Fig. S1C). Subsequently, the $Y^1G^2G^3F^4$ sequence interacted with residues $E231^{5.36}$ and $K235^{5.40}$ near TM5, forming hydrogen bonds with $T220^{ECL2}$ on ECL2 (Fig. S1D). Finally, as shown by structural studies (PDB ID: 8F7Q), $Y^1G^2G^3F^4$ binds stably in the orthosteric pocket through hydrogen bonds and salt bridges with residues $Q126^{2.60}$, $D149^{3.32}$, $H299^{6.52}$, and $W320^{7.35}$ (Fig. S1E). Interestingly, despite exiting the orthosteric pocket *via* the ECL1−ECL3 cleft, β-endorphin's entry point is predominantly aligned with the ECL1/ECL2 interface (Fig. S1C and S1D). This may be attributable to the N-terminal structure partitioning the μ-OR orthosteric pocket entrance into two regions (PDB ID: 5C1M)[32], thereby limiting interactions with ECL3.

To investigate how flexible regions above the orthosteric pocket—ECL1, ECL2, ECL3, and the N-terminal—impact β-endorphin binding and selectivity mechanisms in μ-OR and δ-OR, we performed extensive mutagenesis studies. As a strategy to evaluate wild-type (WT) and mutant μ-OR responses, we employed the G protein-gated inwardly rectifying potassium (GIRK) channel as a reporter, given its established role as a downstream effector of Gβγ subunits[39]. Conventionally, GIRK activity is achieved through co-expression of GIRK1 and GIRK4 subunits[40]. However, a single-point mutation in GIRK4 (S143T)[41] yields a variant, $GIRK4^{S143T}$, which can form functional homotetrameric channels that respond to Gβγ signals upon μ-OR agonist-induced G protein activation[42,43]. This system, coupled with electrophysiological recordings[41], allowed us to directly monitor changes in current amplitudes elicited by OR activation, providing an efficient and precise tool for functional studies (Fig. 2A). In HEK293 cells expressing $GIRK4^{S143T}$ and mORs, β-endorphin-induced currents were recorded for both mμ-OR and mδ-OR (Fig. 2A and B). Consistent with its known non-selective profile, β-endorphin demonstrated similar potency for the two receptor subtypes, with EC_{50} values (the half-maximal effective concentration, indicative of the ligand's potency) of 6.03 ± 3.01 nmol/L for mμ-OR and 7.97 ± 0.87 nmol/L for mouse δ-OR (mδ-OR) (Fig. 2B). In addition, the measured potency for mμ-OR was marginally lower than previously identified values from cAMP inhibition assays (30.2 ± 11.0 nmol/L)[20], supporting the validity of employing $GIRK4^{S143T}$ -based electrophysiological recordings as a reliable approach for studying receptor−ligand interactions.

Interestingly, substituting non-conserved amino acids in the ECL1, ECL2, ECL3, and N-terminal regions of mμ-OR and mδ-OR with residues possessing bulkier side chains to increase steric hindrance resulted in a pronounced μ/δ "selectivity" for β-endorphin (Fig. 2C−E). In mδ-OR mutants $R41^{N\text{-terminal}}W$, $E112^{ECL1}W$, and $V297^{7.32}R$, the potency of β-endorphin for mδ-OR was reduced by 2- to 10-fold ($P = 0.0047$, 0.0001, and 0.0006, respectively; mutations *vs.* WT, two-way ANOVA, Dunnett's multiple comparisons test, F (7, 32) = 15.50; Fig. 2D). Similarly, in mμ-OR mutants $G61^{N\text{-terminal}}W$, $G131^{ECL1}W$, $G131^{ECL1}R$, $T315^{7.32}W$, $T315^{7.32}R$, and $LGG(50-52)^{N\text{-terminal}}WRF$, the potency of β-endorphin for mμ-OR decreased by 10- to 100-fold ($P = 0.0287$, $P < 0.0001$, $P < 0.0001$, $P < 0.0001$, and $P = 0.0111$, respectively; mutations *vs.* WT, two-way ANOVA, Dunnett's multiple comparisons test, F (7, 32) = 15.50; Fig. 2D). These findings underscore the critical role of ECL1 and the N-terminal regions in differential recognition of β-endorphin by mμ-OR and mδ-OR, aligning with the predictions derived from MetaD simulations.

Mutations at equivalent positions with similar chemical properties resulted in varying degrees of reduction in the potency of β-endorphin for mμ-OR and mδ-OR. For example, the potency of β-endorphin for $mδ\text{-}R41^{N\text{-terminal}}W$ was approximately 10-fold lower than that for the $mμ\text{-}P63^{N\text{-terminal}}W$ mutant (Fig. 2E). Conversely, β-endorphin exhibited a 10-fold higher potency for $mδ\text{-}E112^{ECL1}W$ compared to $mμ\text{-}G131^{ECL1}W$ (Fig. 2E). Mutations near TM7 at position 7.32 (7.32W and 7.32R) induced even greater reductions in β-endorphin's potency for mμ-OR (Fig. 2D and E). These findings reveal that β-endorphin, while inherently non-selective between μ- and δ-OR, can "achieve" significant subtype selectivity in the presence of these mutations ($P = 0.0007$, 0.0435, 0.0001, and 0.0486; mutations *vs.* WT; one-way ANOVA, Dunnett's multiple comparisons test, F (7, 16) = 20.28; Fig. 2E).

Notably, these mutated residues are not part of the key amino acids identified in the β-endorphin/hμ-OR complex structure (PDB ID: 8F7Q) that mediate direct interactions with the $Y^1G^2G^3F^4$ motif (*e.g.*, $Q126^{2.60}$, $D149^{3.32}$, $H299^{6.52}$, and $W320^{7.35}$). They also display minimal interaction with the remaining 27 residues of β-endorphin, which form an α-helix. These observations suggest three critical insights: 1) The small side chains and high flexibility of the $Y^1G^2G^3F^4$ motif may allow β-endorphin to traverse the cleft formed by the ECL2/ECL1−N-terminal regions of μ/δ-OR without substantial differentiation in potency due to non-conserved residues. 2) Substituting bulkier side chains into this cleft narrows the μ/δ-OR ECL2/ECL1−N-terminal interface, impeding the uniform access of β-endorphin $Y^1G^2G^3F^4$ to orthosteric pockets of μ/δ-OR, thus conferring relative selectivity. 3) The pathway and geometry of ligand entry, rather than the absolute diameter of the cleft, are the key determinants of selectivity. This mechanism provides an explanation for μ/δ-OR's evolutionary tuning to exhibit negligible selectivity for endogenous β-endorphin while maintaining sharp specificity for EM-1 (see below).

2.2. EM-1's μ/δ-OR selectivity is dictated by non-conserved residues within the orthosteric pocket and ECL

ECL1-3 and N-terminal regions, highly flexible and non-conserved[44] (Supporting Information Fig. S2A−S2C), form receptor-specific extracellular conformations influencing ligand recognition and entry pathways. Structural analyses (PDB IDs: 8F7R[20] and 8EF6[45]) show EM-1 and morphine interact predominantly with residues in transmembrane TM2, TM3, TM5, TM6, and TM7, without engaging ECL1-3 or the N-terminal region (Fig. S2E and S2H). Morphine demonstrates negligible μ/δ-OR selectivity[46] (see below), whereas EM-1 exhibits a pronounced preference for mμ-OR. Electrophysiological data obtained from HEK293 cells expressing μ/δ-ORs and $GIRK^{S143T}$ channels indicated that EM-1 binds mμ-OR with a potency of 1.09 ± 0.13 nmol/L and mδ-OR with a potency of 1708 ± 102 nmol/L, yielding a μ/δ selectivity ratio of 1566-fold (Fig. S2D). These results are consistent with prior radioligand binding studies (1.91 ± 0.13 nmol/L)[20] and previous datasets (2.68 ± 0.28 nmol/L)[47]. The structural basis for this selectivity may be attributed to EM-1's distinct $Y^1P^2W^3F^4$ sequence, which

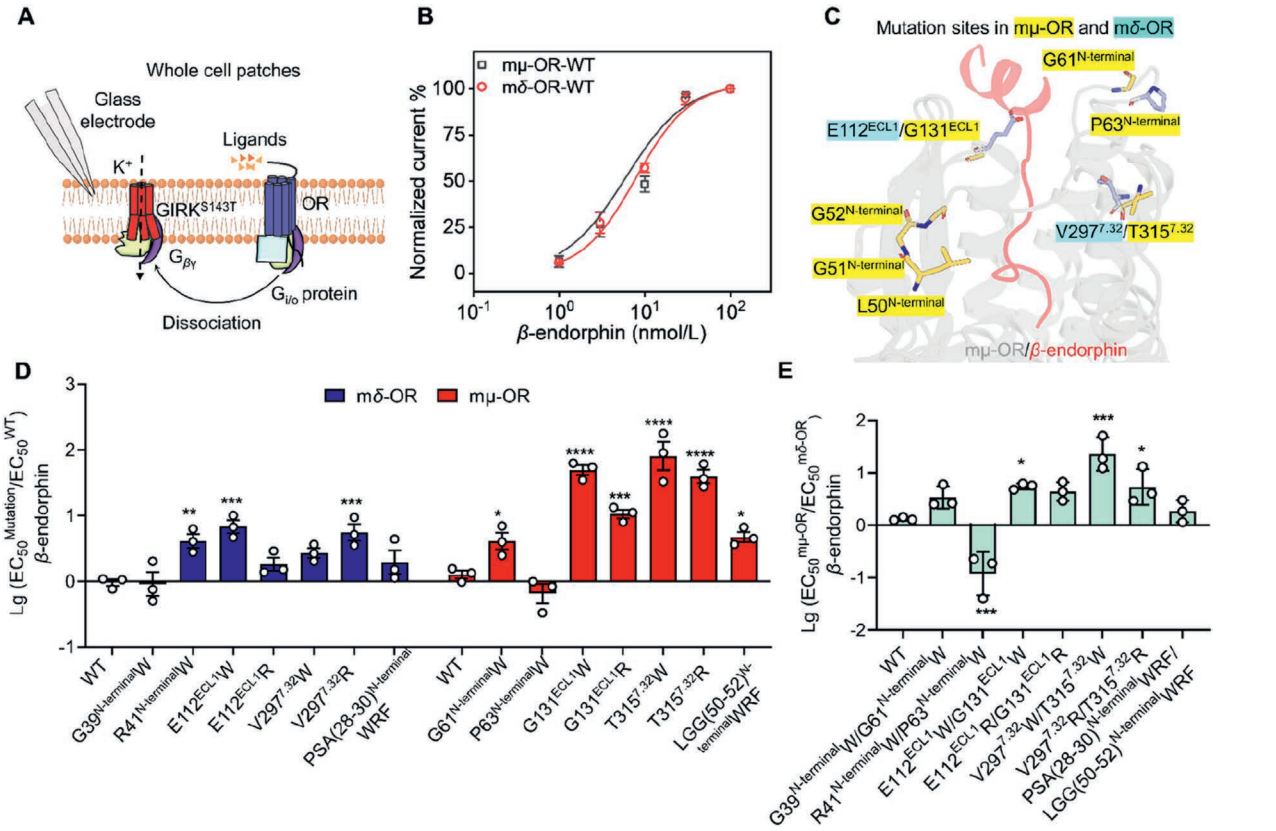

Figure 2 Analysis of N-terminal and ECL1 contributions to β-endorphin binding *via* mutagenesis and GIRK4^{S143T} channel current recordings. (A) Schematic representation of GIRK4^{S143T} channel current detection using whole-cell patch clamp to evaluate receptor activation. (B) Concentration-response analysis of β-endorphin-induced G_i protein activation in mδ-OR-wild type (WT) and mμ-OR-WT. Hill 1 equation fits (solid lines) model the data. Data are presented as mean ± SEM (n = 3). (C) Top-down view of μ-OR and δ-OR mutation sites. Mutation positions are shown as yellow sticks (mμ-OR) and cyan sticks (mδ-OR), with the receptors rendered as gray cartoons. (D) β-endorphin-evoked changes in Gi protein activation detected through GIRK4^{S143T} currents in mutants of mμ-OR (red) and mδ-OR (blue). Bars represent the EC_{50} potency differences of each mutant relative to WT. Statistical significance was assessed using two-way ANOVA with Dunnett's multiple comparisons test (F (7, 32) = 15.50). Significance levels: *P < 0.05, **P < 0.01, ***P < 0.001, ****P < 0.0001. Data are shown as mean ± SEM (n = 3). (E) The relative selectivity of β-endorphin potency (EC_{50}) for μ-OR versus δ-OR, presented as the logarithmic ratio of affinities (Y-axis). WT and site-directed mutations paired with identical positions are shown on the X-axis. Statistical analysis was performed with one-way ANOVA using Dunnett's multiple comparisons test (F (7, 16) = 20.28). Significance levels: *P < 0.05, ***P < 0.001 *vs.* WT. Data are presented as mean ± SEM (n = 3).

contrasts with β-endorphin's $Y^1G^2G^3F^4$. This difference introduces steric hindrance and facilitates the formation of a β-turn in EM-1[20,48,49]. However, whether this remarkable selectivity results from differential accessibility or alternative binding pathways to the μ/δ-OR orthosteric pockets remains an open question.

To elucidate this, we first investigated the role of non-conserved residues within the orthosteric pocket. Conserved residues in μ-OR form the "message" structure of EM-1 (cyan, Fig. S2F), while non-conserved residues in TM2, TM3, and TM7 define the "address" structure (blue and fuchsia, Fig. S2F). The "message−address" paradigm posits that subtype selectivity is dictated by interactions with non-conserved residues within the pocket, with no direct contributions from ECL residues (Fig. S2E). Comprehensive mutagenesis of mδ-OR residues (Supporting Information Fig. S3A, S3B and S3E) implicated in EM-1 binding identified critical determinants of ligand selectivity (Fig. 3A). For instance, the mδ-OR-K108$^{2.63}$N mutation enhanced EM-1 potency by 5.89-fold (EC_{50} reduced from 1708 ± 102 to 290 ± 14 nmol/L, Fig. 3C), while the mδ-OR-L125$^{3.29}$I mutation improved potency by 3.40-fold (EC_{50} reduced to 503 ± 181 nmol/L, Fig. 3C). Furthermore, the K108$^{2.63}$N/L125$^{3.29}$I double mutant exhibited a remarkable 28-fold increase in potency (EC_{50} reduced to 60.9 ± 6.88 nmol/L, Fig. 3C). These findings underscore the critical role of non-conserved orthosteric residues in shaping EM-1 selectivity, reinforcing the "message−address" conceptual framework as a basis for rational drug design and evolutionary studies. Nonetheless, the relatively modest enhancement (28-fold) in selectivity achieved through these mutations suggests that additional, "non-message−address" factors contribute significantly to EM-1's pronounced μ/δ-OR selectivity (1500-fold).

To further elucidate the role of ECL and the N-terminal region in EM-1's μ-/δ-OR selectivity, we engineered chimeric receptors. Non-conserved amino acids within the mμ-OR orthosteric pocket, as well as ECL and N-terminal structures, were replaced with their mδ-OR counterparts to introduce new side chains potentially capable of restoring EM-1 recognition in mδ-OR (Fig. 3D). Among the three chimeras, the $\delta/\mu^{N\text{-terminal}}$ Chimera completely

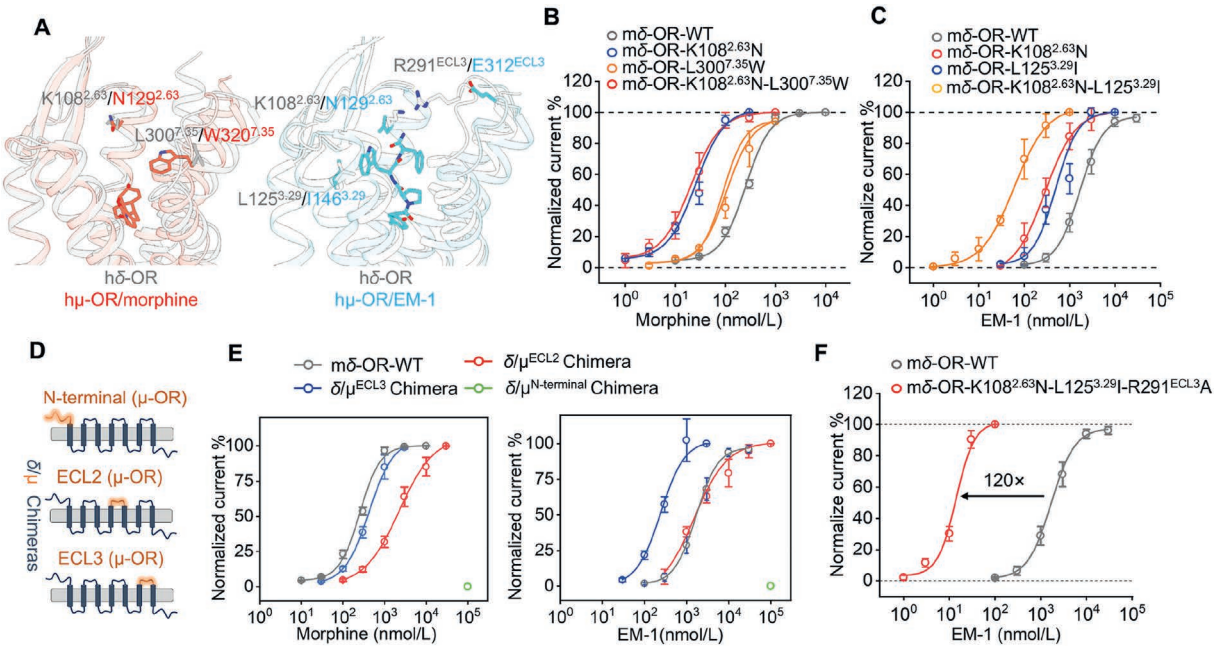

Figure 3 Identification of key residues in μ/δ-OR critical for endomorphin-1 (EM-1) and morphine selectivity. (A) Structural locations of key amino acids in morphine (left, stick, red) and EM-1 (right, stick, blue) distinguishing hμ/δ-ORs (gray cartoon representation). (B, C) Concentration-response curves for G_i protein activation induced by morphine (B) and EM-1 (C) in WT mδ-OR and mutant receptors. Solid lines represent Hill 1 equation fits. Data are shown as mean ± SEM (n = 3−5). (D) Schematic illustration of μ/δ-OR chimeric constructs. The N-terminal, ECL2, and ECL3 regions of δ-OR (navy blue) were sequentially replaced with the corresponding regions of μ-OR (orange). (E) Concentration-response curves for G_i protein activation induced by morphine (left) and EM-1 (right) in WT mδ-OR and μ/δ-OR chimeras. Solid lines indicate Hill 1 equation fits. Data are presented as mean ± SEM (n = 3−5). (F) Concentration-response curves for G_i protein activation induced by EM-1 in WT mδ-OR and the triple mutant mδ-OR-K108$^{2.63}$N-L125$^{3.29}$I-R291^{ECL3}A (3M). The triple mutation increased the potency of EM-1 approximately 120-fold. Solid lines represent Hill 1 equation fits. Data are presented as mean ± SEM (n = 3−5).

abolished EM-1-induced K^+ currents (Fig. 3E). By contrast, the δ/μ^{ECL2} Chimera produced minimal changes in EM-1's potency for mδ-OR (EC_{50} shifted slightly from 1708 ± 102 to 1495 ± 589 nmol/L; Fig. 3E). Notably, the δ/μ^{ECL3} Chimera enhanced EM-1's potency for mδ-OR by 6.9-fold, reducing the EC_{50} to 246 ± 25 nmol/L (Fig. 3E).

These observations suggest that residues within ECL3, in addition to the non-conserved amino acids of the orthosteric pocket, play a pivotal role in EM-1's subtype selectivity. Subsequent analysis pinpointed R291 in ECL3 as a critical determinant of EM-1 binding to mδ-OR. Mutation of this residue (mδ-OR-R291^{ECL3}A) led to a significant improvement in EM-1's potency for mδ-OR, reducing the EC_{50} to 422 ± 69.1 nmol/L (Fig. S3A, S3B and S3E). Combining this mutation with two previously identified gain-of-function mutations (mδ-OR-K108$^{2.63}$N and mδ-OR-L125$^{3.29}$I) yielded the triple mutant mδ-OR-K108$^{2.63}$N-L125$^{3.29}$I-R291^{ECL3}A (3M), which demonstrated a remarkable 120-fold increase in EM-1's potency, reducing the EC_{50} from 1708 ± 102 to 14.2 ± 3.47 nmol/L (Fig. 3F).

To further reinforce our findings, we introduced loss-of-function mutations in mμ-OR at positions corresponding to the gain-of-function mutations observed in mδ-OR. These mutations markedly reduced EM-1's potency for the mμ-OR-N127$^{2.63}$K, mμ-OR-I144$^{3.29}$L, and mμ-OR-E310^{ECL3}R variants by 211-, 6.28-, and 8.94-fold, respectively (EC_{50} values shifted from 1.09 ± 0.13 to 230 ± 51.0 nmol/L, 6.85 ± 0.50 and 9.75 ± 1.67 nmol/L; Supporting Information Fig. S4A and S4B). These data emphasize the indispensable role of specific residues within the orthosteric pocket and ECL1-3 in determining EM-1's potency and μ-/δ-OR selectivity.

2.3. Microscale thermophoresis (MST) and receptor−ligand binding dynamics confirm ECL1's role in EM-1 binding to μ-/δ-OR, independent of G-protein signaling

However, it is important to note that electrophysiological assays of μ-/δ-OR are designed to reflect the potency between ligand and receptor through the activation of downstream GIRK^{S143T} channel. This response could be influenced by enhanced G-protein activation, driven by EM-1-induced conformational changes in the orthosteric pocket, rather than through direct binding or accessibility to the orthosteric site. To rule out this possibility, we performed MST[50] to directly assess the binding affinity of EM-1 for receptor mutants (Fig. 4A). Our results reveal that the binding affinity of EM-1 to mδ-OR-R291^{ECL3}A, mδ-OR-R292^{ECL3}E, mδ-OR-K108^{ECL3}N, and mδ-OR-K108$^{2.63}$N-L125$^{3.29}$I-R291^{ECL3}A increased by 8.56, 7.21, 9.85, and 312-fold, respectively (K_d values from 2945 ± 710 to 344 ± 101, 408 ± 116, 299 ± 72 and 9.42 ± 2.83 nmol/L; Fig. 4A−F), which basically corroborates the electrophysiological data on changes in potency. These results indicate that EM-1 discriminates between mμ-OR and mδ-OR *via* the key residues K108$^{2.63}$, L125$^{3.29}$, and R291^{ECL3}, and this discrimination may be driven by changes in the binding process, rather than through the modulation of G-protein signaling. Specifically, K108$^{2.63}$ and L125$^{3.29}$ directly affect EM-1 binding to mδ-OR, while R291^{ECL3} likely influences ligand access to the receptor's orthosteric pocket, indirectly impacting the EM-1/mδ-OR interaction. This is consistent with the structure of the EM-1/hμ-OR complex (PDB ID: 87FR)[20], where no direct interaction is observed between EM-1 and R291^{ECL3}.

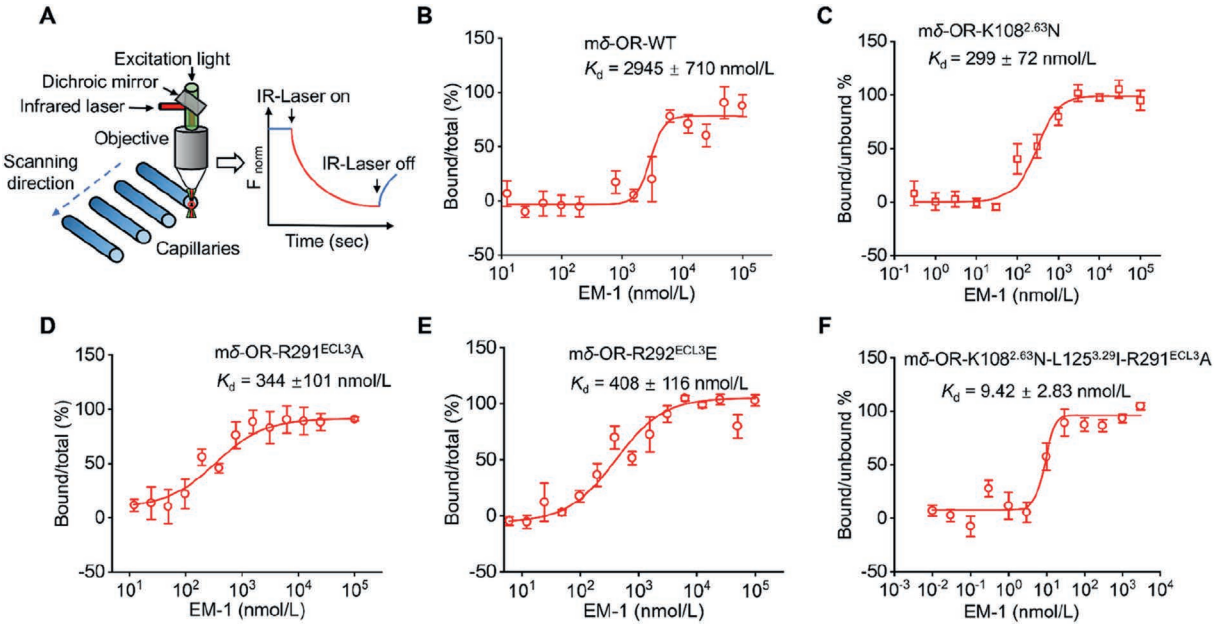

Figure 4 Microscale thermophoresis (MST) assay measuring direct binding of EM-1 to WT and mutant mδ-OR in HEK-293T lysates. (A) Diagram of the MST optical system. MST measurements are conducted in capillaries containing a 10 μL sample volume. Fluorescence excitation and detection are performed through the same optical objective, while a focused infrared laser generates a localized temperature gradient. This gradient induces the thermophoretic movement of fluorescent molecules, which is recorded to quantify molecular interactions. (B−F) MST experiments confirmed direct binding between EM-1 and GFP-tagged WT mδ-OR (B) or its mutant variants (C−F) in HEK-293T cell lysates. (C) Mutants K108$^{2.63}$N, (D) R291^{ECL3}A, (E) R292^{ECL3}E, and (F) K108$^{2.63}$N-L125$^{3.29}$I-R291^{ECL3}A displayed significantly enhanced binding affinity for EM-1 relative to WT mδ-OR.

To deepen our understanding of the dynamic receptor−ligand interactions, we constructed unbiased molecular dynamics simulation systems for both EM-1/hδ-OR and EM-1/hμ-OR and performed a comprehensive 5-μs conventional molecular dynamics (CMD) analysis (Supporting Information Fig. S5A−S5C). After performing extensive conformational sampling over 5 μs, we found that the binding conformations of EM-1 to μ-OR and δ-OR were almost indistinguishable, with the only exception being the differing orientation of the phenyl ring in the Phe^4 side chain (Fig. 5A). This observation implies that the non-conserved amino acids within the binding pocket do not induce subtype selectivity by significantly altering the conformation of EM-1 upon binding. Further interaction analysis between the ligand and receptor revealed that K108$^{2.63}$ (equivalent to N129$^{2.63}$ in hμ-OR) and L125$^{3.29}$ (corresponding to I146$^{3.29}$ in hμ-OR) are key to stabilizing the interaction of EM-1 with hδ-OR (highlighted by solid orange boxes in Fig. S5B and S5C). The variations at these two positions between μ-OR and δ-OR may be central to the μ-/δ-OR selectivity exhibited by EM-1. Importantly, throughout the entire 5 μs CMD sampling, we observed no direct interaction between EM-1 and R291^{ECL3}, which further strengthens the validity of our points regarding the dynamic receptor−ligand interactions.

While the structure of the EM-1/μ-OR complex (PDB ID: 87FR) has been determined[20], the EM-1/δ-OR complex remains uncharacterized. Consequently, it is essential to validate the EM-1/μ-OR structure alongside the homology model for EM-1/δ-OR, as well as the corresponding receptor−ligand interactions obtained from CMD simulations (Fig. 5A−C). Notably, mutations in TM1/4/5 of mδ-OR (Y56$^{1.39}$A, D128$^{3.32}$A, and V217$^{5.43}$A) completely abrogated EM-1's activation of mδ-OR, whereas mutations in TM6 (I277$^{6.51}$A and I304$^{7.39}$A) only minimally affected its activation (Fig. 5B and C). Conversely, alanine substitutions at several TM positions (Y75$^{1.39}$A, N127$^{2.63}$A, Y128$^{2.64}$A, D147$^{3.32}$A, V236$^{5.43}$A, I296$^{6.51}$A, and I322$^{7.39}$A) caused significant reductions in the potency of EM-1 for mμ-OR, indicating that EM-1 extensively occupies the orthosteric pocket of mμ-OR, in line with its high-potency binding profile ($P < 0.0001$, $P < 0.0001$, $P = 0.002$, $P < 0.0001$, $P < 0.0001$, $P < 0.0001$, $P < 0.0001$, mutations *vs.* WT, one-way ANOVA, Dunnett's multiple comparison tests, F (7, 16) = 67.27; Fig. 5D and E). These findings suggest that EM-1's interaction with residues in TM6/7 may be less pronounced during δ-OR activation, indirectly supporting the notion that non-conserved residues in these regions are unlikely to function as key "address" residues for EM-1's subtype selectivity. This is in agreement with the protein−ligand interaction analysis, which showed minimal interaction between EM-1 and non-conserved residues (W284$^{6.58}$ and L300$^{7.35}$) in the TM6/7 helices (Fig. S5B), with corresponding mutations not increasing EM-1's potency for mδ-OR (Fig. S3B and S3E). Thus, the dynamic interactions observed between EM-1 and μ-OR or δ-OR closely correlate with the findings outlined above (Figs. 1−3).

2.4. Non-conserved residues in the orthosteric pocket determine morphine's μ-/δ-OR selectivity beyond the "message−address" model

In the hμ-OR/morphine complex (PDB ID: 8EF6)[45], morphine binds at the bottom of the μ-OR orthosteric pocket, making close contact with TM regions 5, 6, and 7 (Fig. S2H). Like EM-1, the conserved residues at the bottom of the pocket form the "message" that guides morphine binding, while the non-conserved residues in TM5/6/7 might serve as the "address" that

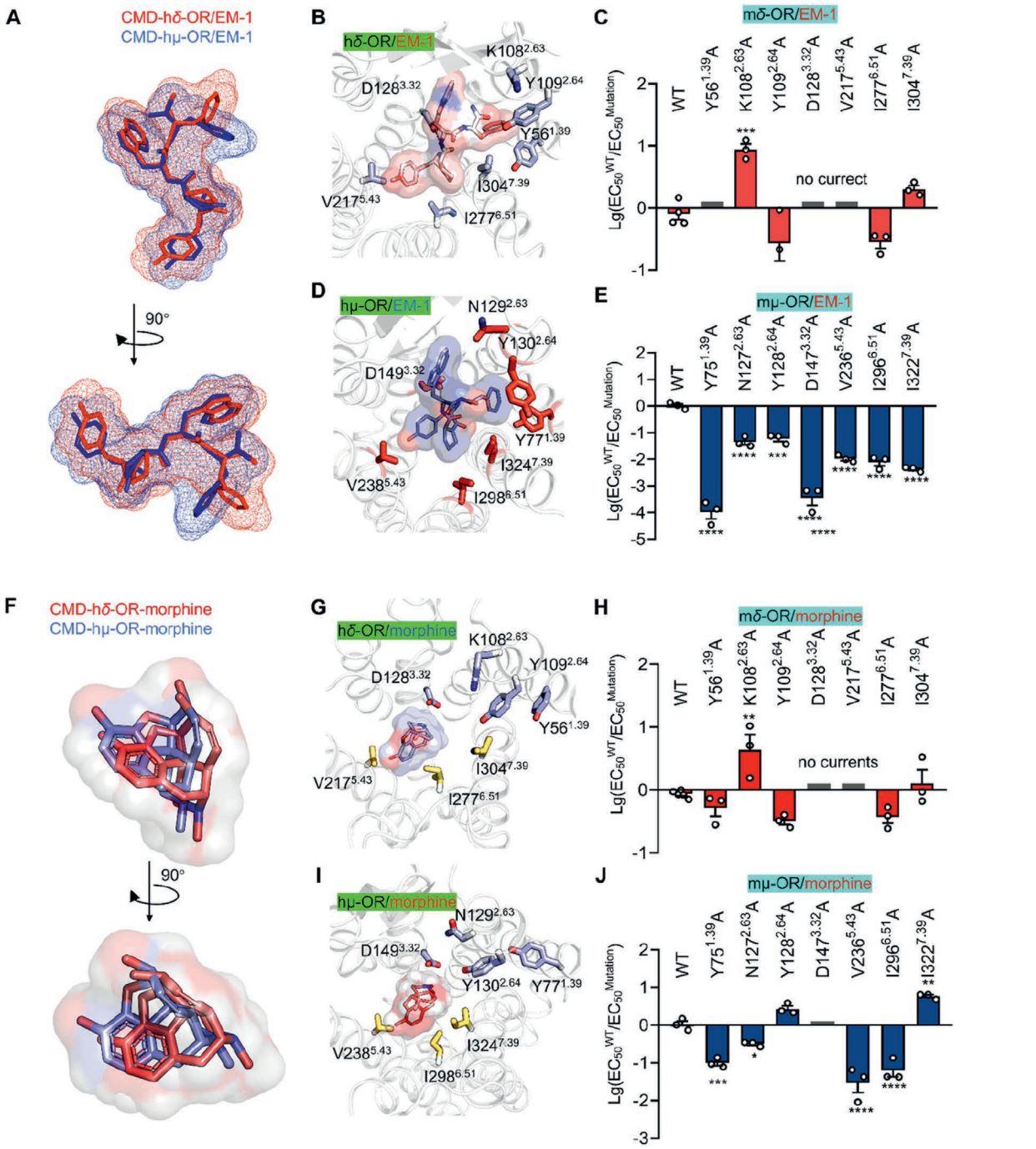

Figure 5 Molecular interactions and functional assays revealing the binding of EM-1 and morphine to μ-OR and δ-OR. (A) Superimposed binding poses of EM-1 in hμ-OR (blue stick) and hδ-OR (red stick) after conventional molecular dynamics (CMD) simulations. (B, D) Structural depiction of molecular interactions between EM-1 and hδ-OR (B) and hμ-OR (D). Key residues mediating interactions with EM-1 and morphine are highlighted as colorful stick representations. (C, E) Functional characterization of G_i protein activation-induced GIRK4^{S143T} channel currents in HEK-293 cells expressing mδ-OR (C) or mμ-OR (E) mutants, activated by EM-1. Potency differences (EC_{50}) of mutants are expressed relative to WT receptors. Statistical analyses: one-way ANOVA with Dunnett's multiple comparisons test; $n = 3$; ***$P < 0.001$, ****$P < 0.0001$ *vs.* WT. *F* values: F (7, 17) [mδ-OR] = 16.43, F (7, 16) [mμ-OR] = 67.27. Data are presented as mean ± SEM. (F) Superimposed binding poses of morphine in hμ-OR (blue stick) and hδ-OR (red stick) after CMD simulations. (G, I) Morphine binding interactions with hδ-OR (G) and hμ-OR (I), with residues participating in interactions visualized as colorful sticks. (H, J) Functional G_i protein activation-induced GIRK4^{S143T} current responses in HEK-293 cells expressing mδ-OR (H) or mμ-OR (J) mutants activated by morphine. Potency differences (EC_{50}) are shown relative to WT receptors. Statistical analyses: one-way ANOVA with Dunnett's multiple comparisons test; $n = 3$; *$P < 0.05$, **$P < 0.01$, ****$P < 0.0001$ *vs.* WT. *F* values: F (7, 18) [mδ-OR] = 8.819, F (7, 16) [mμ-OR] = 46.42.

determines morphine's receptor specificity[45] (Fig. S2I). Morphine has a potency of 12.5 ± 3.52 nmol/L for mμ-OR and 256 ± 27.1 nmol/L for mδ-OR, yielding a relative selectivity of approximately 20.6-fold (Fig. S2G). Using gain-of-function mutagenesis (Figs. S3C, S3D, and S3F), we identified that morphine's μ/δ-OR selectivity is driven by interactions with K108$^{2.63}$ and L300$^{7.35}$ within the mδ-OR binding pocket (Fig. 3A). When K108$^{2.63}$ was mutated to N and L300$^{7.35}$ to W, morphine's potency increased 9.92- and 2.39-fold, respectively (EC_{50} from 256 ± 27.1 to 25.9 ± 4.65, and 140 ± 6.25 nmol/L; Fig. 3B). The double mutation (mδ-OR-K108$^{2.63}$N-L300$^{7.35}$W) resulted in a 12.3-fold increase in potency (EC_{50} from 256 ± 27.1 to 20.7 ± 3.69 nmol/L), narrowing the gap to only 1.67-fold compared to mμ-OR-WT (EC_{50} = 12.4 ± 3.53 nmol/L; Fig. 3B). In our chimera constructs, the $\delta/\mu^{\text{N-terminal}}$ Chimera abolished morphine-induced K^+ currents, while the δ/μ^{ECL2} Chimera decreased morphine's potency for mδ-OR by 8.9-fold (EC_{50} from 256 ± 27.1 to 2267 ± 196.3 nmol/L; Fig. 3E), possibly correlated to impaired binding pathway (see below). The δ/μ^{ECL3} Chimera had a minimal effect on potency (EC_{50} from 256 ± 27.1 to 429 ± 36.1 nmol/L; Fig. 3E). Mutations in mμ-OR-N127$^{2.63}$K and mμ-OR-W318$^{7.35}$L led to a 6.74-and 14.0-fold reduction in morphine's potency, respectively (EC_{50} from 12.4 ± 3.53 to 83.6 ± 32.9, and 174 ± 38.8 nmol/L; Fig. S4C and S4D), suggesting that orthosteric site rather than ECL3 has an impact on morphine's μ/δ selectivity.

To explore the molecular mechanisms behind morphine's interactions with μ-OR and δ-OR, we performed 5 μs of CMD simulations for the morphine/hδ-OR and morphine/hμ-OR complexes (Fig. S5D−S5F). The stable binding conformations of morphine at both receptors were strikingly similar (Fig. 5F, G, and I), which might explain its low selectivity. Morphine formed conserved interactions with D$^{3.32}$ and Y$^{3.33}$ on TM3, as well as hydrophobic interactions with V$^{5.43}$ and I$^{6.51}$ on TM5/6 (Fig. S5E and S5F). Mutations at these sites caused significant reductions in morphine-induced activation (Fig. 5H and J). However, morphine did not interact significantly with the critical selectivity residue K108$^{2.63}$ (corresponding to N129$^{2.63}$ in hμ-OR; Fig. S5E and S5F), as verified by the cryo-EM structure of the hμ-OR/morphine complex (PDB ID: 8EF6)[45] (Fig. S2H). Nevertheless, K108$^{2.63}$ is crucial for morphine's μ/δ selectivity, suggesting that the "message−address" model does not fully explain the molecular basis for this selectivity. Notably, mutations of K108$^{2.63}$ to Ala or Asn increased the potency of both EM-1 and morphine for mδ-OR (Fig. 5C and H), indicating that K108$^{2.63}$, role in selectivity may stem from steric effects rather than direct ligand−residue polar interactions.

2.5. EM-1 utilizes a binding pathway to the orthosteric pocket similarly to β-endorphin's $Y^1G^2G^3F^4$ motif, while morphine follows a different way

The μ/δ-OR selectivity of EM-1, morphine, and β-endorphin challenges the simplistic "message−address" hypothesis within the orthosteric pocket (Figs. 2−5). Interactions between amino acids from the ECL and N-terminal regions possibly influence the accessibility of the orthosteric pocket, thereby modulating receptor selectivity. Additionally, ECL3 plays a critical role in EM-1's binding to the δ-OR orthosteric pocket, contributing additional subtype selectivity, while its influence on morphine's binding to δ-OR is minimal (Fig. 3E). Thus, we propose that morphine and EM-1 adopt distinct binding pathways to δ-OR, which accounts for their contrasting μ/δ-OR selectivity. To explore this further, we employed MetaD simulations, performing enhanced sampling on hμ-OR/morphine (CV1, the distance between the hydroxyl oxygen of D149$^{3.32}$ and N2 of morphine; CV2, the distance between the Cα of W295$^{6.48}$ and N2 of morphine, Supporting Information Fig. S6A) and hμ-OR/EM-1 (CV1, the distance between the hydroxyl oxygen of D149$^{3.32}$ and N8 of EM-1; CV2, the dihedral angles formed by Cα^{Y1}, Cα^{P2}, Cα^{W3}, and Cα^{F4}, of EM-1, Fig. S6B). These MetaD simulations revealed distinct pathways for morphine and EM-1 to bind to the receptor orthosteric pocket (Fig. S6A and S6B): morphine enters *via* a large gap between ECL2 and TM5 (Fig. 6A and C), while EM-1 enters through a smaller gap formed by ECL3, ECL1, and the N-terminal (Fig. 6B and C). This difference may explain why morphine's binding to the receptor is not influenced by ECL3.

To validate our hypothesis further, we designed engineered zinc bridges to modify the binding pathways of EM-1 and morphine into mδ-OR (Fig. 6D and E). The zinc bridge, formed by interactions between Zn^{2+} ($ZnCl_2$) and histidine[51-53], stabilizes receptor conformation and prevents ligand entry. A wealth of structural studies establishes that the canonical zinc coordination with histidine nitrogen typically features a bond angle close to ∼95−110° and a bond length around 1.95−2.25 Å[53,54]. We constructed closed-state models of mδ-OR-Q190$^{\text{ECL2}}$H/-Q201$^{\text{ECL2}}$H and mδ-OR-S45$^{\text{N-terminal}}$H/E112$^{\text{ECL1}}$H, in which the initial zinc-bridge geometries conformed well to the canonical bond angles and lengths[52] (Fig. S6C). Throughout 1.2 μs of CMD simulations, the NE2(Q201$^{\text{ECL2}}$H)-Zn^{2+}-NE2(Q190$^{\text{ECL2}}$H) coordination angle consistently fluctuated within ∼105−109° (Fig. S6D). The distances betweenNE2(Q201$^{\text{ECL2}}$H)-Zn^{2+} and Zn^{2+}-NE2(Q190$^{\text{ECL2}}$H) remained stably around 2.2 and 2.3 Å, respectively, while the Cβ−Cβ distance between Q201$^{\text{ECL2}}$H-Q190$^{\text{ECL2}}$H fluctuated steadily around 7.7 Å (Fig. S6E) suggesting robust coordination of Zn^{2+} by NE2 atoms of both histidine substitutions. Furthermore, the side-chain dihedral angles (Cα-Cβ-Cγ-ND1) of Q201$^{\text{ECL2}}$H and Q190$^{\text{ECL2}}$H maintained consistent values near 120 and 50°, respectively (Fig. S6F), indicating conformational stabilization upon zinc coordination. Similarly, the stability of the engineered zinc bridge between S45$^{\text{N-terminal}}$H and E112$^{\text{ECL1}}$H was evaluated *via* a 1.2 μs CMD simulation (Fig. S6G). The NE2(S45$^{\text{N-terminal}}$H)-Zn^{2+}-NE2(E112$^{\text{ECL1}}$H) bond angle, the Cβ−Cβ distance between S45$^{\text{N-terminal}}$H and E112$^{\text{ECL1}}$H, and the NE2−Zn^{2+} coordination distances all remained highly stable, fluctuating within 107−111°, ∼9.5, ∼2.2, and ∼2.4 Å, respectively (Fig. S6H and S6I). The dihedral angles (Cα−Cβ−Cγ−ND1) of both residues also persisted near 120 and 60° (Fig. S6J), indicating that coordination with Zn^{2+} constrained their conformational flexibility. Collectively, these findings suggest that our engineered zinc bridges fulfill key valence geometry criteria and represent structurally plausible coordination complexes.

Next, in the mδ-OR-Q190$^{\text{ECL2}}$H/Q201$^{\text{ECL2}}$H double mutant, the zinc bridge formed by Q190$^{\text{ECL2}}$H and Q201$^{\text{ECL2}}$H residues reduced morphine-induced GIRK$^{\text{S143T}}$ currents by approximately 80%, without affecting EM-1's activation of mδ-OR (Fig. 6D, P = 0.0005, unpaired t-test; $ZnCl_2$, 1 mmol/L). In contrast, in the mδ-OR-S45$^{\text{N-terminal}}$H/E112$^{\text{ECL1}}$H double mutant, the zinc bridge between S45$^{\text{N-terminal}}$H and E112$^{\text{ECL1}}$H reduced EM-1-induced GIRK$^{\text{S143T}}$ currents by about 50%, but had no effect on morphine activation of mδ-OR (Fig. 6E, P = 0.0016, unpaired t-test). 1 mmol/L $ZnCl_2$, as a control, did not alter EM-1 or morphine activation of WT mδ-OR, mδ-OR-Q190$^{\text{ECL2}}$H,

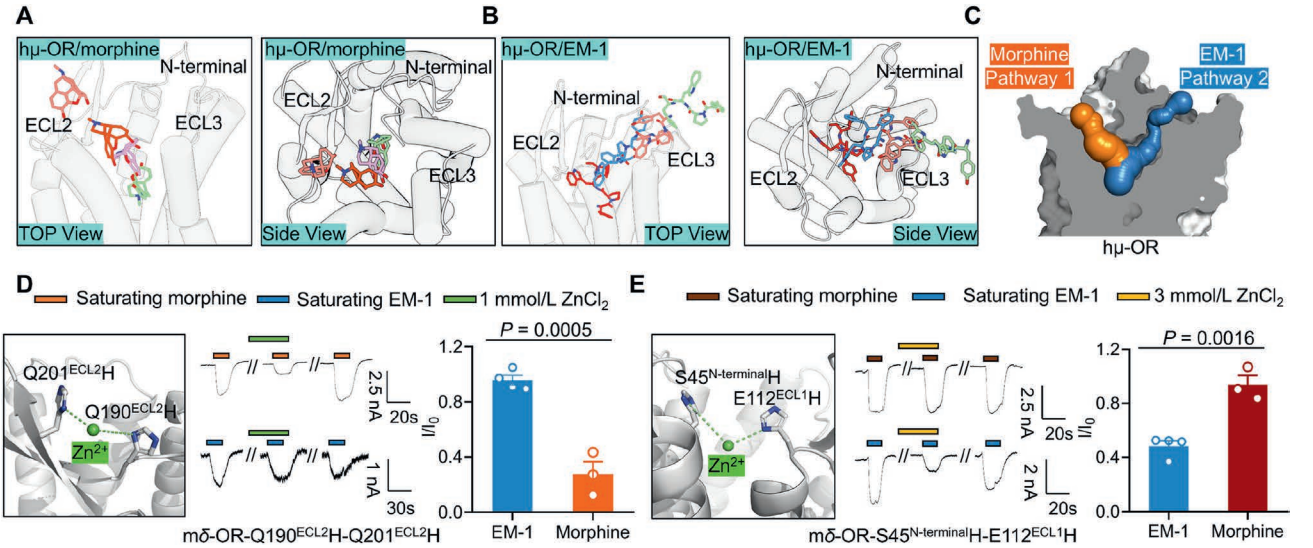

Figure 6 Morphine and EM-1 possibly utilize distinct pathways to access the orthosteric pocket of ORs. (A) Morphine accesses the orthosteric pocket of hμ-OR through a cleft between ECL2 and TM5, as shown in the top (right) and side(left) views. Morphine is represented as sticks, and the receptor structure as a cartoon. (B) EM-1 follows a distinct pathway, entering the hμ-OR orthosteric pocket through a cleft formed by the N-terminal domain and ECL3, illustrated in top (left) and side (right) views. EM-1 is represented as sticks, and the receptor as a cartoon. (C) Visualization of the two binding pathways for morphine (orange) and EM-1 (blue). Pathway 1 (morphine) exhibits a greater average radius compared to pathway 2 (EM-1). (D) Zinc coordination between $Q201^{ECL2}H$ and $Q190^{ECL2}H$ forms an artificial zinc bridge (left). Representative whole-cell patch clamp recordings (middle) and pooled data (right) demonstrate ligand-induced $GIRK4^{S143T}$ currents in mδ-OR-$Q190^{ECL2}H$-$Q201^{ECL2}H$ transfected cells upon treatment with morphine (>10 μmol/L) or EM-1 (>1 μmol/L)) in $ZnCl_2$ (1 mmol/L). Current ratios before and after $ZnCl_2$ treatment are shown. Each data point corresponds to an independent cell (n = 3−4). Statistical comparison: EM-1 *vs.* morphine, unpaired *t*-test. Data are presented as mean ± SEM. (E) Zinc coordination between $S45^{N\text{-terminal}}H$ and $E112^{ECL1}H$ create a similar zinc bridge (left). Whole-cell patch clamp recordings (middle) and pooled data (right) show ligand-induced currents in mδ-OR-$S45^{N\text{-terminal}}H$-$E112^{ECL1}H$-transfected cells in the presence of $ZnCl_2$ (3 mmol/L). Data represent current ratios before and after $ZnCl_2$ treatment. Each point represents a cell (n = 3−4). Statistical comparison: EM-1 *vs.* morphine, unpaired *t*-test. Data are presented as mean ± SEM.

mδ-OR-$Q201^{ECL2}H$ (Supporting Information Fig. S7A−S7C); 3 mmol/L $ZnCl_2$ did not alter EM-1 or morphine activation of mδ-OR-$S45^{N\text{-terminal}}H$, mδ-OR-$E112^{ECL1}H$ (Fig. S7D and S7E). Stabilization of ECL2 by the engineered zinc bridge hindered morphine binding to mδ-OR, suggesting a significant interaction between morphine and ECL2 before entering the orthosteric pocket. Conversely, stabilization of N-terminal-ECL1 blocked EM-1 binding to mδ-OR, highlighting a prominent interaction between EM-1 and the N-terminal during the binding process.

Additionally, mutating mδ-OR-$Q201^{ECL2}$ to Arg, increasing steric hindrance, reduced morphine's potency by approximately 3.82-fold (EC_{50} from 256 ± 27.1 to 980 ± 180 nmol/L, Fig. S7F), while EM-1's potency for mδ-OR-$Q201^{ECL2}R$ increased by approximately 1.45-fold (EC_{50} from 1708 ± 102 to 1172 ± 13 nmol/L, Fig. S7F). Deletion of the larger steric group mδ-OR-$R291^{ECL3}$ resulted in a 4.62-fold increase in EM-1's potency for mδ-OR (EC_{50} from 1708 ± 102 to 369 ± 15 nmol/L, Fig. S7F), whereas morphine's potency increased by 1.36-fold (EC_{50} from 256 ± 27 to 188 ± 24 nmol/L, Fig. S7F and S7G). The $Q201^{ECL2}R$ mutation had a more substantial impact on morphine binding (P = 0.0025, EM-1 *vs.* morphine, two-way ANOVA, Sidak's multiple comparison tests, F (2, 15) = 5.080; Fig. S7G), while the $R291^{ECL3}$ deletion mutation more notably affected EM-1 binding (P = 0.0448, EM-1 *vs.* morphine, two-way ANOVA, Sidak's multiple comparisons test, F (2, 15) = 5.080; Fig. S7G). These findings from engineered zinc bridge and site-directed mutagenesis support the point that EM-1 and morphine may utilize distinct pathways to access the mδ-OR orthosteric pocket.

2.6. Morphine and EM-1 induce distinct conformational changes in extracellular flexible regions of the mδ-OR upon binding to the orthosteric pocket

To bolster the evidence of their entry into the orthosteric pocket and to illuminate their interactions with ECL and N-terminal regions during binding, we utilized unnatural flUAA insertion coupled with VCF analysis. The flUAA 3-(6-acetylnaphthalen-2-ylamino)-2-aminopropanoic acid (Anap) is a noncanonical amino acid endowed with an environment-sensitive fluorescent group, the emission wavelength of which shifts in response to alterations in solvent polarity[55,56]. Changes in conformation at the Anap site or in adjacent residues, which affect the local hydrophobicity, lead to a corresponding shift in the maximum absorption wavelength (Fig. 7A and B). A stop codon (TAG) was introduced at specific residues of mδ-OR (ECL1: M111, F116; ECL2: D193, Q201; TM6: W284; ECL3: V287, R291, R292), and Anap was incorporated through tRNA-CUA and tRNA synthetase-specific insertion (Fig. 7C and D). Compared to EM-1, morphine binding to mδ-$D193^{ECL2}$TAG and mδ-$D201^{ECL2}$TAG resulted in a more pronounced shift in the maximum emission wavelength of Anap (P = 0.0483 and 0.0015, respectively, EM-1 *vs.* morphine, two-way ANOVA, Sidak's multiple comparisons test, F (7, 131) = 10.11; Fig. 7E and F). Conversely, when mδ-OR-$R291^{ECL3}$TAG and mδ-OR-$R292^{ECL3}$TAG was activated, EM-1 caused a more significant shift in the maximum emission wavelength of Anap compared to morphine (P < 0.0001, P < 0.0001, EM-1 *vs.* morphine, Sidak's multiple comparison tests, F (7,

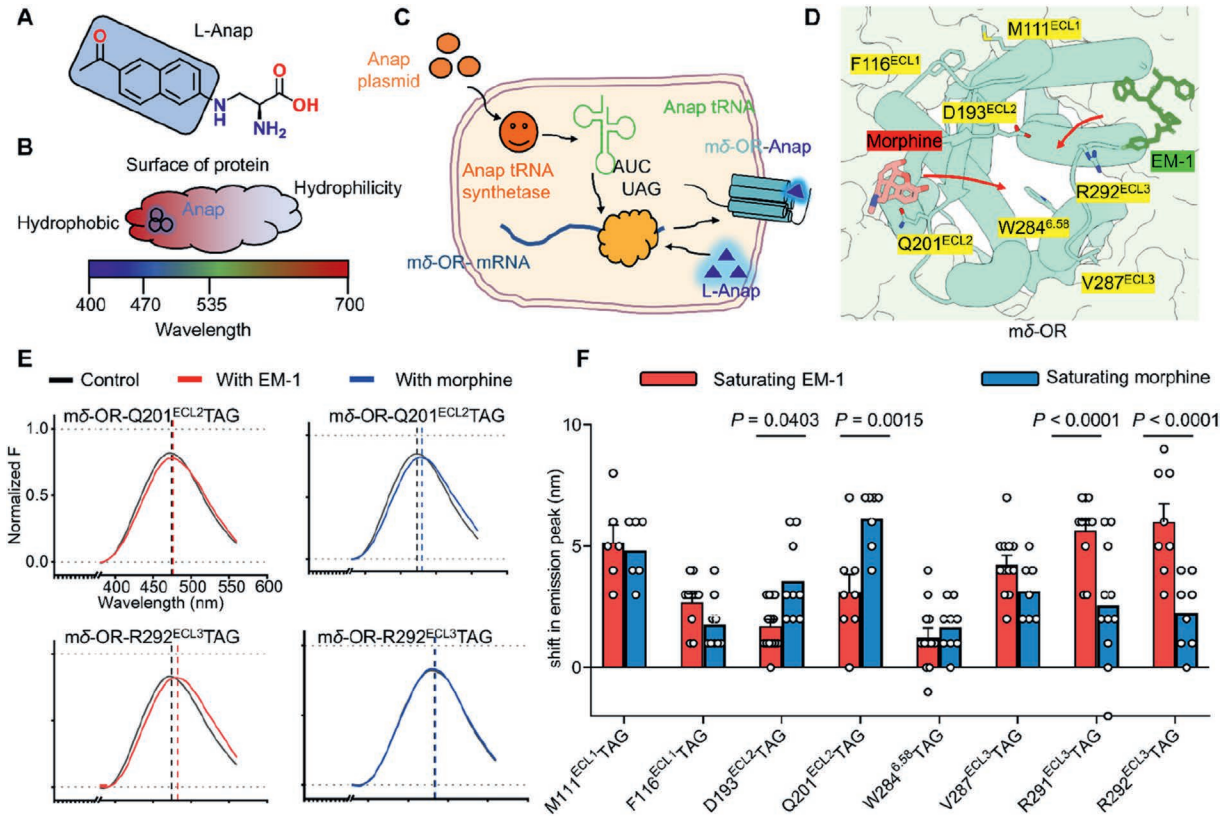

Figure 7 Fluorescent unnatural amino acid (flUAA) incorporation and voltage-clamp fluorometry (VCF) reveal distinct conformational changes during mδ-OR activation by EM-1 and morphine. (A) The molecular structure of L-Anap, the flUAA employed. (B) A diagram illustrating the effect of local hydrophilicity changes on the emission spectrum of L-Anap. (C) The approach used to incorporate L-Anap into specific sites within the mδ-OR structure. (D) Top view of the receptor, showing L-Anap integrated into the ligand-binding pathway. Red arrows indicate the respective binding pathways of EM-1 (green) and morphine (pink). (E) Emission peak shifts observed with L-Anap at residues 201 (ECL2) and 292 (ECL3) in response to saturating EM-1 (red) or morphine (blue) compared to bath solution (black). (F) Quantitative analysis of emission peak shifts under ligand treatment. Data points (shown as circles) represent mean ± SEM from $n = 6-14$ independent experiments. Statistical analysis was performed using two-way ANOVA with Sidak's multiple comparisons test (F (7, 131) = 10.11).

131) = 10.11; Fig. 7E and F). These results suggest that the distinct Anap signal variations elicited by morphine and EM-1 reflect their capacity to induce divergent conformational changes in specific regions of the receptor. Morphine primarily drives notable conformational alterations in ECL2, whereas EM-1 exhibits a stronger interaction with ECL3, consistent with their respective binding mechanisms.

2.7. Combined N-terminal substitution and triple mutation K108$^{2.63}$N/L125$^{3.29}$I/R291^{ECL3}A in mδ-OR enhance EM-1 potency to levels comparable with WT mμ-OR

The N-terminal structure plays a critical role in embedding the orthosteric pockets in both mδ-OR and mμ-OR (Fig. 8A), while also partitioning the ligand entry pathways[32] into distinct regions (Fig. 6A–C). This indicates that the N-terminal may interact synergistically with different ECLs to modulate ligand access to the orthosteric pocket. Although altering the size of N-terminal amino acid side chains can "reclaim" μ/δ-OR selectivity for the non-selective peptide β-endorphin, introducing N-terminal chimeras in studies involving EM-1 and morphine resulted in receptor dysfunction (Fig. 3E). To refine our understanding of the N-terminal's essential role in μ/δ-OR selectivity, we took a more cautious strategy by replacing N-terminal residues near TM1 every three amino acids, generating five triple mutants. The mδ-OR-PSA(28–30)-LGG mutant, in particular, increased the EC_{50} for EM-1 by 4.39-fold (from 1728 ± 102 to 389 ± 25.9 nmol/L, Fig. 8B), with other mutants showing modest increases in potency.

Next, we incorporated N-terminal modifications into the mδ-OR-3M mutant (K108$^{2.63}$N/L125$^{3.29}$I/R291^{ECL3}A), achieving an EM-1 potency of 8.4 ± 0.23 nmol/L, a remarkable 203-fold improvement over WT mδ-OR (Fig. 8C), and only 7.71-fold lower than WT mμ-OR. MST analysis further confirmed a direct binding affinity of 1.03 ± 0.48 nmol/L for EM-1 to the mδ-OR-3M-PSA(28–30)-LGG mutant, a 2859-fold increase compared to the WT receptor (Fig. 8D). The enhanced binding of EM-1 to mδ-OR with N-terminal modifications highlights the pivotal role of the N-terminal in shaping EM-1's subtype selectivity. A significant shift in the emission wavelength of the Anap group inserted at the S37$^{N\text{-terminal}}$ position provides further evidence of a substantial conformational change in the N-terminal upon EM-1 binding ($P = 0.0002$, unpaired t-test; Fig. 8E and F).

The data presented herein suggest that the non-conserved N-terminal and ECL3 regions are critical contributors to the selective recognition of EM-1, primarily through steric constraints imposed on its bulkier side chains during receptor engagement. Conversely, these selectivity-conferring regions appear ineffective in discriminating the flexible β-endorphin, which possesses

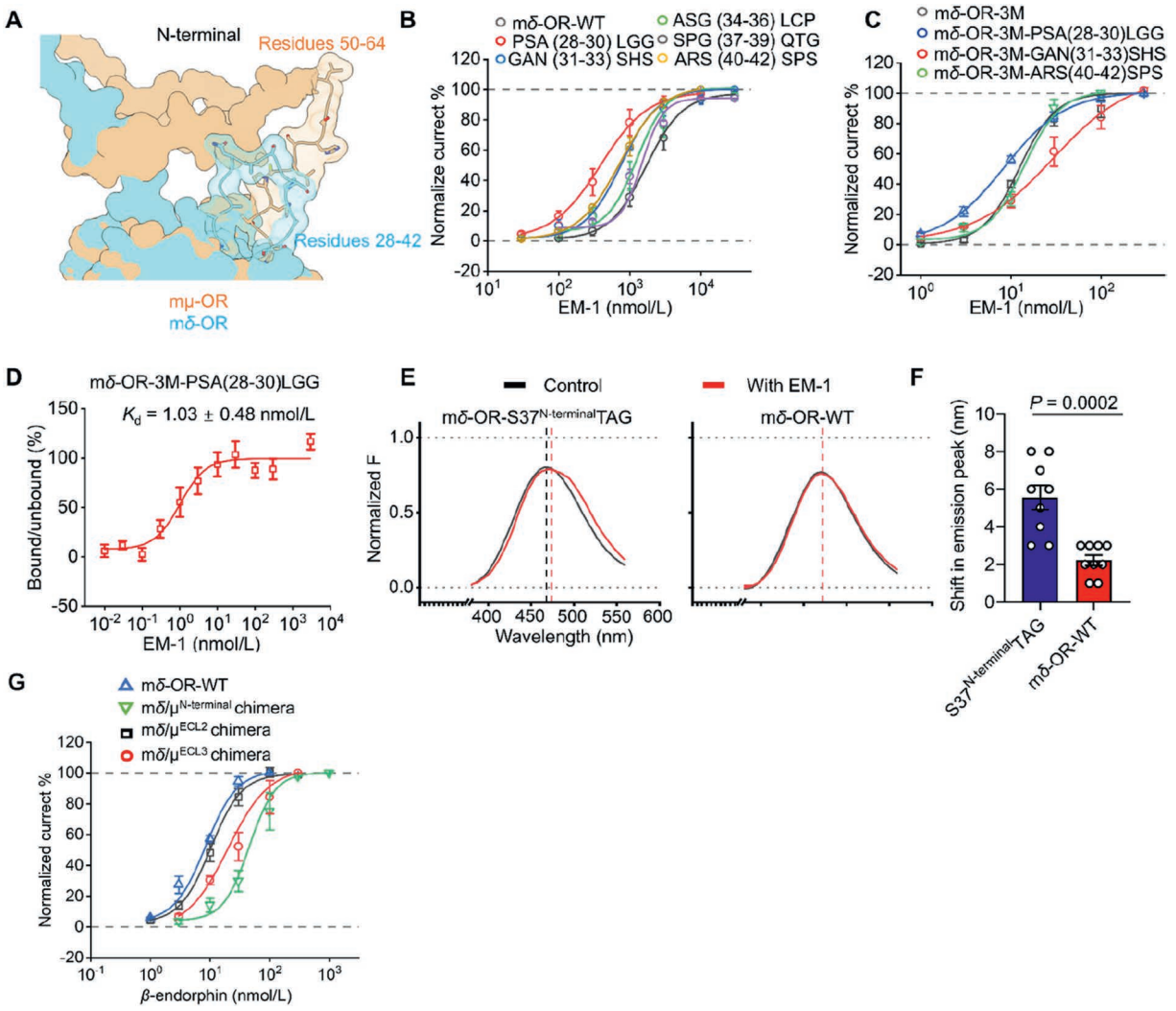

Figure 8 Impact of the N-terminal on the binding dynamics of EM-1 to mδ-OR and mμ-OR. (A) Side view of the homology models for the N-terminal regions of mμ-OR (orange) and mδ-OR (blue), based on the BU72/mμ−OR complex (PDB ID: 5C1M). (B, C) Concentration−response curves for G_i protein activation induced by EM-1 in WT mδ-OR and N-terminal mutants. The solid lines represent the fits to the Hill 1 equation (n = 3−5). Data are expressed as mean ± SEM. (D) MST analysis detecting direct binding between eGFP-tagged mδ-OR-3M-PSA (28−30) LGG and EM-1 in lysates from HEK293T cells expressing the tagged receptor. (E) Representative shifts in the emission peak observed in HEK293T cells transfected with mδ-OR-S37$^{\text{N-terminal}}$TAG and mδ-OR WT. Data points: black (bath solution), red (saturating EM-1). (F) Pooled emission peak shift data for mδ-OR-S37$^{\text{N-terminal}}$TAG versus WT mδ-OR following saturating EM-1 treatment. Statistical analysis was performed using an unpaired t-test. Data are presented as mean ± SEM, with individual data points shown as circles. (G) Concentration-response curves for G_i protein activation induced by β-endorphin in WT mδ-OR and mδ/$\mu^{\text{N-terminal}}$, mδ/μ^{ECL2} and mδ/μ^{ECL3} chimeras. The solid lines represent the fits to the Hill 1 equation. Data are expressed as mean ± SEM (n = 3).

smaller side chains and a more adaptable sequence. Consistent with this, β-endorphin activates mδ/$\mu^{\text{N-terminal}}$ chimera, mδ/μ^{ECL2} chimera, mδ/μ^{ECL3} chimeras with EC_{50} values of 10.3 ± 0.9, 20.2 ± 5.2, and 45.8 ± 6.9 nmol/L, respectively (Fig. 8G), representing approximately one-, two-, and five-fold decreases in efficacy relative to the wild-type receptor. The pronounced (>1500-fold) disparity in EM-1 potency between mμ-OR and mδ-OR (Fig. S2E) further substantiates the notion that β-endorphin's flexibility and reduced steric hindrance render the receptor domain swaps insufficient to induce significant μ/δ subtype selectivity.

To explore the ligand−N-terminal interactions in greater detail, we employed the BU72/mμ-OR (PDB ID: 5C1M) model to supplement partial N-terminal sequences in the EM-1-hμ-OR, morphine-hμ-OR, and β-endorphin-hμ-OR systems, followed by CMD simulations. The key amino acids involved in persistent interactions between EM-1, morphine, and hμ-OR were consistent with the results of the initial CMD simulations (Supporting Information Figs. S5 and S8). Notably, morphine forms transient water-bridging and hydrogen-bonding interactions with residue D56 of the N-terminal (yellow solid line box, Fig. S8A), a similar interaction seen in the BU72−mMOR complex[32]. In contrast, EM-1 showed minimal detectable interactions with the N-terminal (Fig. S8B). These findings suggest that the N-terminal, similar to ECL3, contributes to the specific conformation that defines the EM-1 binding pathway, influencing pocket accessibility without altering the stable binding state of EM-1 to the receptor.

Finally, correct plasma membrane localization and expression are prerequisites for the functional performance of membrane proteins[57-59]. To eliminate the confounding effects of altered receptor surface expression on functional outputs, we systematically evaluated current density (pA/pF)[60,61]—an established proxy for membrane protein abundance—across key mutants and chimeric constructs. Leu-enkephalin (Leu-ENK, 10 μmol/L), a full agonist, was used at saturating concentration to activate mδ-OR and its variants (Supporting Information Fig. S9A). Mutants $L125^{3.29}I$, $K108^{2.63}N$, $L300^{7.35}W$, $R291^{ECL3}A$, $K108^{2.63}N$-$L125^{3.29}I$, $K108^{2.63}N$-$L125^{3.29}I$-$R291^{ECL3}A$ (3M), 3M-PSA(28−30)-LGG, $K108^{2.63}N$-$L300^{7.35}W$, and chimeras such as mδ/μ(ECL2) and mδ/μ(ECL3) all exhibited maximum currents statistically indistinguishable from wild-type receptor (one-way ANOVA, F (11, 46) = 3.815, Fig. S9A). The only construct demonstrating significantly attenuated current amplitude was the mδ/μ(N-terminal) chimera ($^*P < 0.05$, Fig. S9A). These results imply that, with the exception of the N-terminal chimera, the observed functionality of the mutants is not attributable to differential surface expression.

To rigorously validate the membrane localization of the receptors, we isolated membrane proteins from HEK293T cells, encompassing both plasma membrane components and proteins from other intracellular membranes, employing a commercially available membrane and cytosol protein extraction kit (Beyotime Biotechnology, P0033)[62,63]. All remaining mutants and chimeras exhibited membrane expression levels comparable to that of the WT receptor, with the $L125^{3.29}I$ mutant even showing a modest increase, indicating intact receptor trafficking to the plasma membrane ($^*P < 0.05$; mutants and chimeras *vs.* WT, one-way ANOVA, F (11, 35) = 4.226; Fig. S9B and S9C). Notably, despite reduced current density, the mδ/μ(N-terminal) chimera displayed no detectable difference in membrane expression relative to WT, suggesting that its diminished maximal response may arise from altered ligand accessibility or activation-associated conformational dynamics.

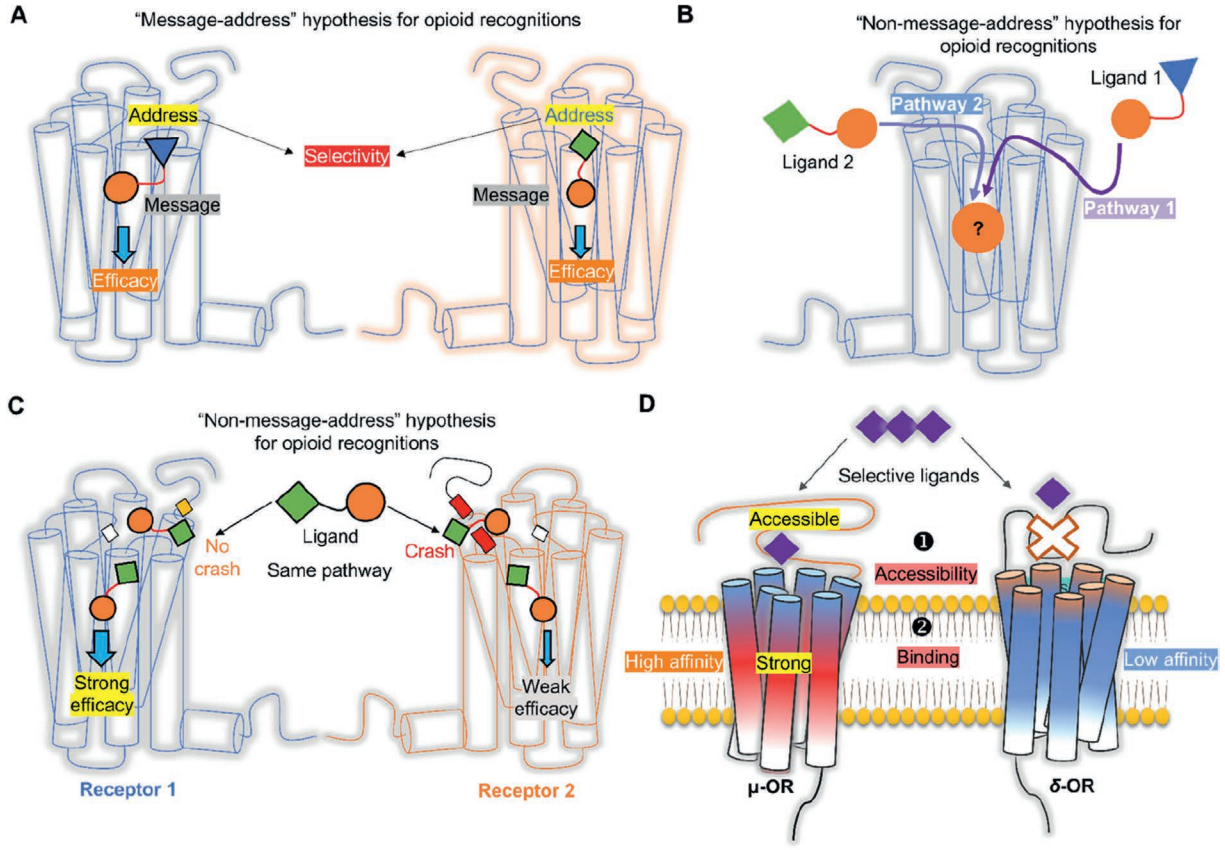

Figure 9 Mechanism of ligand selectivity in μ- and δ-opioid receptors *via* the "non-message−address" paradigm. (A) Diagram illustrating the contributions of the "message" and "address" motifs in opioid receptor ligand recognition. The "message" structure (gray) engages conserved amino acids at the receptor binding pocket's base, facilitating receptor activation. Meanwhile, the "address" structure (yellow) interacts with non-conserved amino acids at the top of the pocket, playing a crucial role in ligand selectivity. (B, C) Overview of the "non-message−address" model of ligand binding. Ligands follow distinct pathways with varying accessibility to the receptor binding pocket (B). Arrows indicate the different routes through which ligands bind. Ligands may utilize the same pathway to bind to different receptor subtypes; however, interactions with non-conserved amino acids along these pathways limit ligand accessibility and lead to diverse receptor activation profiles (C). Non-conserved amino acids are indicated by yellow and red squares. (D) Schematic of the ligand−receptor binding process, highlighting its two stages: "entry" and "binding". High-affinity ligands rapidly and efficiently access the receptor binding pocket (left, red), while low-affinity ligands struggle to enter (right, blue). In the second stage, high-affinity ligands bind tightly and strongly activate the receptor, whereas low-affinity ligands result in weaker binding and activation.

3. Discussion

The "message−address" theory not only guides the design and synthesis of opioid receptor-selective ligands, but also provides a comprehensive framework for understanding the ligand−receptor recognition patterns and activation mechanisms[18,20-22,64,65], thereby advancing our knowledge of opioid receptor signal transduction. Ligand−receptor binding is a dynamic and continuous process[66] (Fig. 9A). However, the "message−address" theory primarily describes the stable binding state between ligands and receptors, overlooking the dynamics of the binding process itself[28] (Fig. 9B and C). Our data reveal that the selective binding of EM-1 to opioid receptors is influenced not only by non-selective amino acids in the binding pocket, but also by non-conserved residues in ECLs (Fig. 3). The effect of $R291^{ECL3}$ on EM-1 binding cannot be explained by the "message−address" theory (Fig. 3F), as no direct interaction between EM-1 and $R291^{ECL3}$ is observed in the hμ-OR/EM-1 complex structure (PDB ID: 8F7R)[20] (Fig. S2E). Similarly, while the $K^{2.63}$ residue in the binding pocket is primarily responsible for the μ/δ selectivity of morphine (Fig. 3B), there is no direct or evident interaction between this site and morphine (Fig. S2H), further challenging the "message−address" model. Previous studies of opioid receptor ligand selectivity have focused mainly on non-conserved amino acid residues that directly interact with ligands in the binding pocket[18,19,67], with less emphasis on the role of non-conserved regions above the pocket. Through analysis of the hμ-OR/β-endorphin complex (PDB ID: 8F7Q) and site-directed mutagenesis, we propose that ligands adopt specific binding paths to interact with opioid receptors, and that the binding process is modulated by non-conserved amino acids in the flexible regions of ECL1, ECL2, ECL3, and the N-terminal. To explore further how regions above the binding pocket contribute to ligand subtype selectivity, we examined two ligands—EM-1 and morphine—that fully occupy the orthosteric pocket. Using chimeric constructs and extensive site-directed mutagenesis, we identified key amino acid residues that influence the μ/δ-OR selectivity of both ligands. The highly selective EM-1 distinguishes μ-OR from δ-OR by relying on $K^{2.63}$ and $L^{3.29}$ in the binding pocket, and non-conserved residues in ECL3 and the N-terminal. In contrast, the less selective morphine relies on the $K^{2.63}$ residue in the binding pocket. Our methods, including MetaD and CMD conformational sampling, artificial zinc bridge construction, and flUAA Anap insertion and VCF analysis, reveal that β-endorphin, EM-1, and morphine follow distinct, narrow or broad pathways to reach the orthosteric pocket, offering new insights into μ/δ-OR selectivity. This "non-message−address" selective mechanism refines and complements the "message−address" theory of the μ/δ-OR orthosteric pocket.

Ligands may adopt different binding paths to interact with receptors, depending on their molecular structure, as exemplified by EM-1 and morphine (Fig. 9B). Alternatively, the same ligand may follow a similar binding path for a specific receptor subtype, but variations in accessibility and conformational changes induced by non-conserved amino acids along the binding path might lead to differences in ligand binding and distinct agonistic effects[68] (Fig. 9C). Whether such variations exist remains to be further investigated, such as the possibility of subtle differences between EM-1 and β-endorphin that affect downstream functionality in mμ-OR. Therefore, the ligand-OR orthosteric pocket interactions can be divided into two stages—entry and binding—that together influence ligand affinity, selectivity, and downstream effects. First, ligands enter the receptor's binding pocket *via* specific pathways, with accessibility varying across receptor subtypes, affecting ligand affinity. Second, ligands bind stably in a specific conformation, with binding influenced by the selectivity determined by non-conserved amino acids in the pocket (Fig. 9D). Our data show that flexible regions above the orthosteric pocket could affect ligand binding. For example, the chimeric construct mδ-OR-$K108^{2.63}$N/$L125^{3.29}$I enhances the potency of EM-1 for mδ-OR by approximately 28-fold (Fig. 3C). Further introduction of ECL3 residues in mδ-OR-$K108^{2.63}$N-$L125^{3.29}$I-$R291^{ECL3}$A (3M) increases EM-1's potency by approximately 120-fold (Fig. 3F). Adding N-terminal residues in mδ-OR-3M-PSA(28−30)LGG elevates EM-1's potency to 8.4 ± 0.23 nmol/L, a 203-fold increase compared to mδ-OR-WT (Fig. 8C), which is only 7.71 times weaker than EM-1's potency for mμ-OR-WT. Additionally, MST measurements show that the direct binding affinity of EM-1 for mδ-OR-3M-PSA(28−30)LGG is 1.03 ± 0.48 nmol/L, a 2859-fold increase compared to WT (Fig. 8D), suggesting that the amino acids in ECL3 and the N-terminal are crucial for determining the accessibility and μ/δ-OR selectivity of EM-1.

The "non-message−address" mechanism elucidated here may also apply to ligand recognition and binding in other class A GPCRs (Class B and C GPCRs may differ in mechanism due to differences in N-terminal length and three-dimensional architecture[44]), including other endogenous opioid peptides such as enkephalin, endorphin, dynorphin and nociceptin, and their corresponding receptor subtypes[13,69,70]. The evolutionary mechanisms driving selectivity in these peptides remain unclear. Non-selective enkephalins and endorphins share a common N-terminal sequence ($Y^1G^2G^3F^4$) and adopt specific binding paths to the opioid receptor's orthosteric pocket. Due to their small side-chain structure and greater flexibility, these peptides pass through the "filter" formed by non-conserved amino acids in the ECL1-3 and N-terminal regions, resulting in a lack of receptor selectivity[20]. In contrast, dynorphins, which are selective for κ-OR and share the $Y^1G^2G^3F^4$ structure, exhibit $\kappa/\mu/\delta$ selectivity ratios of 1:120:174[20,71]. Endogenous peptides like EM-1 ($Y^1P^2W^3F^4$) and EM-2 ($Y^1P^2F^3F^4$) show more than 1500-fold μ/δ subtype selectivity[31] (Fig. S2D). This likely results from evolutionary reductions in peptide length and increases in the N-terminal side chain size, which enhance selectivity by allowing these larger side chains to interact more strongly with the "filter" of non-conserved residues in the ECL1-3 and N-terminal regions. Thus, selectivity in endogenous peptide ligands may be largely encoded by the "YXXF" motif at the N-terminal that enters the orthosteric pocket. Additionally, modifying the first amino acid of the $Y^1G^2G^3F^4$ motif to $F^1G^2G^3F^4$ results in nociceptin, a σ-OR-selective ligand[20,72,73]. Exogenous high-selectivity peptide ligands, such as DAMGO(Y^1-{D-Ala}^{2}-G-{Me-Phe}^{3}-G-ol^4)[74] and deltorphin ($Y^1A^2F^3E^4V^5V^6G^7$)[75], can also be engineered by modifying the side-chain structure of the YXXF motif. The mechanisms underlying receptor subtype selectivity for these ligands are still being elucidated.

The binding pathways of EM-1, morphine, and β-endorphin are defined by intricate molecular interactions and structural dynamics, warranting detailed discussion. The $Y^1G^2W^3F^4$ sequence of EM-1 follows a binding path similar to that of β-endorphin in the hμ-OR/β-endorphin complex[20] (Fig. 6B), with β-endorphin likely entering the binding pocket from the ECL1-N-terminal region (Fig. 1D and Figs. S1−S4). In contrast, EM-1 engages the orthosteric pocket *via* a cleft delineated by the N-terminal region and ECL3 (Fig. 6B and C). Morphine diverges further, entering the orthosteric pocket through a broader region spanning ECL2

and TM5 (Fig. 6A and C). These pathways are governed by the interplay between the ligands' molecular properties and the extracellular conformational dynamics of the receptor. For β-endorphin, its $Y^1G^2G^3F^4$ sequence, characterized by smaller side chains and greater flexibility (Fig. 1D), ensures an unimpeded path through the ECL1-N-terminal interface to the orthosteric pocket of μ-OR or δ-OR. In contrast, the bulkier side chains of EM-1's $Y^1P^2W^3F^4$ motif result in pronounced accessibility differences (Fig. S2E), allowing EM-1 to enter μ-OR through the N-terminal-ECL3 cleft. However, the ECL3 region of mδ-OR, enriched in arginine residues, imposes greater resistance, explaining EM-1's μ/δ selectivity exceeding 1500-fold. Morphine, with its rigid polycyclic core and isoquinoline scaffold and wider lateral radius (Fig. S5D), utilizes the expansive ECL2−TM5 region as its entry point (Fig. 6A and C). The absence of marked accessibility differences in this region between μ-OR and δ-OR likely underlies morphine's limited subtype selectivity. The distinct binding pathways of these three ligands are shaped by three critical factors: (1) the semi-embedded architecture of the μ/δ-OR orthosteric pocket, (2) the bifurcation of the entry point by the N-terminal region, and (3) the differential spatial constraints posed by linear peptides versus rigid small molecules. Importantly, ligand access to the orthosteric pocket is not solely determined by the size or diameter of the entry point but rather by the comprehensive structural characteristics of the binding pathway. This structural complexity fine-tunes ligand selectivity, as evidenced by side-chain modifications influencing μ/δ-OR selectivity in varied and ligand-specific ways (*e.g.*, β-endorphin; Fig. 2).

Despite significant advances in structural biology[18-20,32,36,45,76], the full architecture of the opioid receptor N-terminal region remains unresolved in most ligand−receptor complexes. This gap in structural information limits our understanding of the N-terminal's role in ligand recognition, receptor binding, activation, and downstream signal transduction. Opioid receptor ligands encompass a diverse repertoire, including endogenous short and long peptides, exogenous small molecules like morphine, and emerging biased ligands. Our findings demonstrate that these ligands induce conformational changes in the N-terminal and ECL regions, modulating binding affinity and functional selectivity. As loosely coupled proteins, GPCRs transmit subtle differences in ligand binding into distinct downstream signaling responses[15]. Thus, investigating the dynamic interplay between ligands and GPCRs, particularly focusing on orthosteric pocket accessibility in μ/δ-OR, provides a promising strategy for the rational design of functionally selective and subtype-selective ligands.

Finally, reducing the adverse effects of opioid analgesics remains a primary focus of drug development[77]. Although μ-OR-targeted drugs exhibit unparalleled analgesic potency, their severe side effects stemming from receptor hyperactivation constrain their clinical utility. Emerging studies highlight the potential of multitarget ligands that engage multiple opioid receptor subtypes, achieving robust analgesia with reduced side effects[78]. Dual μ-OR/κ-OR agonists like oxycodone[79] and κ-OR agonists with μ-OR antagonistic properties like dezocine[80] exemplify this approach. While these agents lack high subtype selectivity, their complementary pharmacological effects mitigate adverse outcomes. Additionally, G protein-biased μ-OR agonists, such as TRV130[81], Tegileridine[82], retain analgesic efficacy while minimizing side effects[83]. These findings underscore that both functional and subtype selectivity are crucial for improving the safety profile of opioid therapeutics. Designing bivalent ligands with functional bias, such as dual μ/κ-OR agonists[4,78], represents a promising avenue for next-generation opioid analgesics.

4. Conclusions

In conclusion, the "non-message−address" selectivity mechanism proposed herein augments the classical "message−address" theory by elucidating an additional layer of complexity in μ/δ-OR orthosteric pocket interactions. This mechanism not only deepens our understanding of the evolutionary underpinnings of endogenous peptide selectivity but also provides a conceptual framework for designing innovative opioid ligands with improved efficacy and reduced side effects. Comprehensive elucidation of the structural and molecular determinants underlying subtypes and functional selectivity, including the "non-message−address" mechanism described here, will be instrumental in guiding the development of safer and more effective opioid therapeutics.

5. Experimental

5.1. Chemical agents and mutagenesis

All compounds were purchased from Sigma−Aldrich (St. Louis, USA) except for endomorphin-1 (Aladdin, China), β-endorphin (Aladdin, China). The plasmid mμ-OR-pIRES2-eGFP, mδ-OR-pIRES2-eGFP, mμ-OR-eYFP-pcDNA3.1$^+$, mμ-OR-eGFP-pcDNA3.1$^+$ are constructed through homologous recombination and confirmed by DNA sequencing. The plasmid-containing AnapRS and the corresponding tRNAs were generously provided by Dr. Wei Yang (School of Medicine, Zhejiang University, China). All mutations and chimeras were generated with the KOD-Plus-Mutagenesis Kit and confirmed by DNA sequencing.

5.2. Cell culture and electrophysiology

Human embryonic kidney (HEK-293) cells were cultured in DMEM medium adding 1% penicillin/streptomycin (Gibco), 1% glutamate (Gibco) and 10% FBS (PAM) at 37 °C in a humidified atmosphere of 5% CO_2 and 95% air. The plasmids of mμ-OR, mδ-OR and GIRK4^{S143T} was transiently co-transfected in HEK293 cells in a ratio 2:0.5 with the transfection agent containing two types of solutions (solution A contains 250 mmol/L $CaCl_2$ in pure water; solution B contains (in mmol/L) 1.5 Na_2HPO_4, 140 NaCl, and 50 HEPES, and pH was adjusted to 6.96).

All electrophysiological recordings were performed at room temperature (23 ± 2 °C) with Axon200B on HEK293 cells after at least 24 h transfection[84]. The conventional whole-cell configuration was performed under the voltage clamp with a holding potential of −60 mV. Patch pipettes had a resistance ranging from 3 to 5 MΩ when filled with intracellular solution containing (in mmol/L) 30 NaCl, 0.5 $CaCl_2 \cdot 2H_2O$, 10 HEPES, 120 KCl, 1 $MgCl_2 \cdot 6H_2O$ and 5 EGTA with pH adjusted to 7.4 by Tris-base. Throughout the whole-cell recordings, cells were bathed in the standard external solution containing (in mmol/L) 150 NaCl, 5 KCl, 10 glucose, 2 $CaCl_2 \cdot 2H_2$ O, 10 HEPES and 1 $MgCl_2 \cdot 6H_2O$ with pH being adjusted to 7.4. The high concentration of K^+ solution contained (in mmol/L) 155 KCl, 10 glucose, 2 $CaCl_2 \cdot 2H_2O$, 10 HEPES and 1 $MgCl_2 \cdot 6H_2O$ with pH being adjusted to 7.4 by KOH, and was used to induce the inward current of GIRK4^{S143T} channel. All agonists were dissolved and

diluted by the standard external solution. Membrane current signals were amplified by a patch clamp amplifier (Axon200B, Axon Instruments, Foster City, CA, USA) with low-pass filtering at 1 kHz using low-pass Bessel filters and 0.5 of output gain (α) (low-pass filter at 2 kHz and 50 of output gain (α) for single-channel recordings). A Digidata 1440B interface and a computer running the Clampex and Clampfit 10.6 software (Molecular Devices) were used to sample and analyze all currents.

5.3. *Fluorescent unnatural amino acid (flUAA) incorporation and the voltage-clamp fluorometry (VCF) analysis*

As we previously described[85], HEK293T cells were cultured in a medium supplemented with 20 μmol/L L-Anap (AsisChem Inc.). The plasmid containing AnapRS, the corresponding tRNA, and receptor plasmids carrying wild-type (WT) or mutated genes were co-transfected into cells using Lipofectamine® 3000 reagents. The Anap-added medium was changed every 8 to 24 h and then replaced with L-Anap-free culture medium for 24 h to fully express the channel prior to the experiment.

Anap fluorescence was excited by a wLS LED light source (PHOTOMETRICS, Tucson, USA) using BP340−390 excitation filters, DM410 dichroic filters and BA420-IF emission filters. The emission spectra of Anap were captured using an Acton SpectraPro SP-2150 spectrometer (Princeton Instruments) and a Prime 95 B CCD camera (Photometrics), and the emission peak value was found by fitting the spectrum with a tilted Gaussian distribution[55]. Briefly, the emission spectra of individual cells before and after administration of μ-OR ligands, were recorded with the use of an excitation filter of 340−390 nm (UV). For each cell, the maximum intensity was determined after subtracting the background, and the emission intensities at individual wavelengths were normalized to the maximum intensity. After fitting with the Gaussian equation, the peak emission wavelength was determined as the wavelength corresponding to the peak of the Gaussian curve. A shift in the peak emission wavelength (in nm) before and after agonist or antagonist administration reflects a conformational change in and near the ANAP-incorporated site induced by the drug and was used for quantification.

5.4. *Microscale thermophoresis test (MST)*

As previously described[86,87], MST experiments were performed using Monolith NT.115 (Blue/Red) instrument (NanoTemper Technologies GmbH, Germany). The cell lysates of HEK293T cells expressing mμ-OR-eGFP were used as a source of fluorescently labeled mμ-OR. HEK293T cells were transfected with GFP-fused mμ-OR WT and mutants, and lysed 24 h after transfection. Cells were collected by centrifugation and pellets were included in PBS 20 mmol/L, EDTA 2 mmol/L, protease inhibitors (PI), for 30 min on ice. The sample is homogenized using an ultrasonic disruptor and centrifuged 10 min 400 × g at 4 °C. Supernatants were centrifuged 45 min at 20,000 × g at 4 °C to pellet membrane fragments. The pellets were then collected in a smaller volume with PBS, tween 0.05%, PI in order to obtain a total protein concentration of 10 mg/mL, as controlled by bicinchoninic acid assay (BCA) for each sample. Samples were stored at −80 °C before use. All dilutions were prepared to ensure that no other gradient (salt, glycerol, DMSO, etc.) was created during buffer mixing. To minimize adsorption of the sample to material, low retention tips and tubes were used, and Tween 20 at 0.05% was added to the PBS, buffer used to dilute all components. After mixing the sample with the compound in a 1:1 ratio, the samples were incubated at room temperature for 2 h before loading into standard capillaries (NanoTemper Technologies GmbH, MO-K022). The LED power was set to 20% and MST power to "medium". Hill model was used to evaluate binding affinity; each data point represents mean △Fnorm values from four-six independent experiments. The bound fraction of the mμ-OR-eGFP was determined and the fitting was performed using the Hill 1 model method incorporated by the MO Affinity Analysis v2.3 software (NanoTemper Technologies).

5.5. *Surface expressions of mδ-OR mutants*

HEK293T cells expressing either the wild-type or site-directed mutant variants of mδ-OR were washed three times with ice-cold phosphate-buffered saline (PBS) to remove residual medium and debris. Membrane proteins, comprising both plasma membrane components and proteins associated with other intracellular membrane systems, were subsequently extracted using the Cell Membrane and Cytoplasmic Protein Extraction Kit (Beyotime) in strict accordance with the manufacturer's instruction[62,63]. The membrane protein fractions were solubilized in SDS sample buffer and resolved *via* SDS−polyacrylamide gel electrophoresis (SDS−PAGE), followed by transfer onto PVDF membranes. Membranes were blocked with 5% non-fat dry milk for 1−2 h at ambient temperature and incubated overnight at 4 °C with primary antibodies targeting Oprd or Na^+/K^+−ATPase, prepared in 5% milk. Following multiple washes (4−5 times) with Tris-buffered saline containing Tween-20 (TBST), membranes were treated with horseradish peroxidase-conjugated secondary antibodies for 2 h at room temperature. Protein bands were visualized using enhanced chemiluminescence (ECL, Thermo), and images were captured using the Tanon 5200 Multi chemiluminescence imaging system with an exposure duration of 1−3 min. Quantitative densitometric analyses were performed with ImageJ software, based on data collected from no fewer than three independent biological replicates.

5.6. *Stimulations and opioid receptor modeling*

Although multiple μ-OR structures exist, high-resolution full-length models are lacking. We employed a multi-template approach using the mouse μ-OR/BU72 crystal structure (5C1M, residues 52−64) combined with human μ-OR cryo-EM structures bound to EM-1 (8F7R), morphine (8EF6), and β-endorphin (8F7Q). Structural and sequence alignment allowed accurate reconstruction of human μ-OR ligand-bound coordinates. The N-terminal domain was modeled based on 5C1M, followed by localized energy minimization of the N-terminal segment and adjacent residues with MODELLER[88]. Multiple models underwent Ramachandran validation[89,90]; the model with the highest percentage of residues in allowed conformations was selected for subsequent experimental and simulation studies.

The energy-minimized models of hμ-OR/EM-1, hμ-OR/morphine, hμ-OR/β-endorphin, hμ-OR/EM-1-N-terminal, hμ-OR/morphine-N-terminal, hμ-OR/β-endorphin-N-terminal were used as the initial structures for molecular simulations. A large 1-palmitoyl-2-oleoyl-*sn*-glycero-3-phosphocholine (POPC, 300K) bilayer, available in System Builder of DESMOND[91], was built to generate a suitable membrane system based on the OPM database (https://opm.phar.umich.edu)[92], in which the TM domain of the μ-OR could be embedded properly. The hμ-OR/EM-1/POPC, hμ-OR/morphine/POPC, hμ-OR/β-endorphin/POPC, hμ-OR/EM-1-

N-terminal/POPC, hμ-OR/morphine-N-terminal/POPC, hμ-OR/β-endorphin-N-terminal/POPC system was dissolved in simple point charge (SPC) water molecules. Counterions were then added to compensate for the net negative charge of the system. NaCl (150 mmol/L) was added into the simulation box that represents background salt at physiological condition. The DESMOND default relaxation protocol was applied to each system prior to the simulation run. Briefly, (1) 100 ps simulations in the NVT (constant number (N), volume (V), and temperature (T) ensemble with Brownian kinetics using a temperature of 10 K with solute heavy atoms constrained; (2) simulations were performed for 12 ps in the NVT ensemble using a Berendsen thermostat at 10 K with small-time steps and solute heavy atoms constrained. (3) 12 ps simulations in the NPT (constant number (N), pressure (P), and temperature (T) ensemble using a Berendsen thermostat and barostat for 12 ps simulations at 10 K and 1 atm, with solute heavy atoms constrained; (4) 12 ps simulations using a Berendsen thermostat and Barostat at 300 K and 1 atm, with solute heavy atoms constrained; (5) 24 ps simulations using a Berendsen thermostat and Barostat at 300 K and 1 atm, with no constraints. After equilibration, the MD simulations were carried out for about 5 μs. The long-range electrostatic interactions were calculated using the smooth particle grid Ewald method. The trajectory recording interval was set to 500-ps and the other default parameters of DESMOND were used in the conventional molecular dynamics (CMD) simulation runs[93]. All simulations used the OPLS 2005 all-atomic force field[94-96], which is used for proteins, ions, lipids and SPC waters. The Simulation Interaction Diagram (SID) module in DESMOND[51,97] was used to explore the interaction analysis between morphine/EM-1/β-endorphin and μ-OR.

The default relaxation protocol of DESMOND was applied to each system before metadynamics (MetaD)[37] simulations were run (same steps as for CMD simulations, see above). The parameters for height, width of the Gaussian, and the interval were set to 0.03 kcal/mol, 0.05 Å and 0.09 ps, respectively. All metadynamics simulations were run for 120 ns until they showed free diffusion along the defined CV. Gaussian sums and free energy surfaces were generated by DESMOMD's metadynamics analysis tool. The bias $V(s, t)$ is typically constructed in the form of periodically added repulsive Gaussians, where s is the chosen CV which could be multidimensional. Therefore, the free-energy surface (FES) can be constructed in the space spanned by those C*Vs*. The bias potential $V(s, t)$ at time t can be written as Eq. (1)[98-100]:

$$V(s,t) = \int_0^t \omega \, exp\left(- \sum_{i=1}^{d} \frac{(S_i - S_i(t'))^2}{2\sigma_i^2} \right) dt' \quad (1)$$

where ω is the Gaussian height controlled by the deposition stride, S_i is one of d CVs, and σ_i is the Gaussian width. This method pushes the system to escape the local minima to find the nearest saddle point on the FES. When the transient happens, the bias provides the free-energy estimate as Eq. (2):

$$V(s,t) = -F(S) + C \quad (2)$$

where C is an arbitrary additive constant. Since the absolute free energy is normally not important, this constant can be readily eliminated for calculating the free-energy difference.

All MD simulations were performed in DELL T7920 armed by NVIDIA TESLTA K40C or CAOWEI 4028 GR armed by NVIDIA TESLTA K80. The simulation system was prepared, trajectory analyzed and visualized on a CORE DELL T7500 graphics workstation with 12 CPUs.

5.7. Data analysis

Electrophysiological recordings were analyzed with Clampfit 10.6 (Molecular Devices). Pooled data were expressed as mean ± standard error of mean (SEM). Statistical comparisons were conducted using Student's *t*-test, one-way ANOVA analysis or two-way ANOVA analysis, where significance levels were denoted as $^{*}P < 0.05$, $^{**}P < 0.01$, $^{***}P < 0.001$ or $^{****}P < 0.0001$. All data used to construct concentration-response relationships originated from the same experimental group. Data were fitted to the Hill 1 equation.

Acknowledgments

This work was supported by Changsha "Jie Bang Gua Shuai" Major Science and Technology Programs (KQ2301004, China), National Natural Science Foundation of China (U23A20524, 32371289), the CAMS Innovation Fund for Medical Sciences (CIFMS)(2019-I2M-5-074, China), Innovation and Entrepreneurship (Shuangchuang) Program of Jiangsu Province (JSSCTD202350, China), the China Postdoctoral Science Foundation (2023M733896), and the Medical ResearchImprovement Project of Lanzhou University (lzuyxcx-2022-156, China), 'Xing Yao' Leading Scholars of China Pharmaceutical University (2021).

Author contributions

Ye Yu designed the project. Xin Zhang, Hong Yan Song, and Ruo Fan Chen performed patch-clamp recording. Xin Zhang and Ye Yu performed homology modeling and simulations. Xin Ran Kong, Hong Yan Song performed cell culture and made mutations. Ruo Fan Chen, Xin Zhang and Hong Yan Song performed the data analysis and visualization. Ye Yu, Xing Hua Li and Jin Wang supervised the project. Xin Zhang, Hong Yan Song, Ruo Fan Chen and Ye Yu provided the method. Ye Yu and Xin Zhang wrote the manuscript.

Conflicts of interest

The authors have no conflicts of interest to declare.

Appendix A. Supporting information

Supporting information to this article can be found online at https://doi.org/10.1016/j.apsb.2025.11.039.

References

1. Congreve M, de Graaf C, Swain NA, Tate CG. Impact of GPCR structures on drug discovery. *Cell* 2020;**181**:81−91.
2. Stein C. Opioid receptors. *Annu Rev Med* 2016;**67**:433−51.
3. Darcq E, Kieffer BL. Opioid receptors: drivers to addiction?. *Nat Rev Neurosci* 2018;**19**:499−514.
4. Hovah ME, Holzgrabe U. Bivalent and bitopic ligands of the opioid receptors: the prospects of a dual approach. *Med Res Rev* 2024;**44**: 2545−99.
5. Vidal-Torres A, Fernández-Pastor B, García M, Ayet E, Cabot A, Burgueño J, et al. Bispecific sigma-1 receptor antagonism and μ-opioid receptor partial agonism: WLB-73502, an analgesic with improved efficacy and safety profile compared to strong opioids. *Acta Pharm Sin B* 2023;**13**:82−99.

6. Faouzi A, Varga BR, Majumdar S. Biased opioid ligands. *Molecules* 2020;**25**:4257.
7. Kenakin T. Biased receptor signaling in drug discovery. *Pharmacol Rev* 2019;**71**:267−315.
8. Jastrzębski MK, Wójcik P, Grudzińska A, Andreozzi G, Vetrò T, Asim A, et al. Biased signaling *via* serotonin 5-HT_{2A} receptor: from structural aspects to *in vitro* and *in vivo* pharmacology. *Acta Pharm Sin B* 2025;**15**:4438−55.
9. Mallipeddi S, Janero DR, Zvonok N, Makriyannis A. Functional selectivity at G-protein coupled receptors: advancing cannabinoid receptors as drug targets. *Biochem Pharmacol* 2017;**128**:1−11.
10. Raehal KM, Schmid CL, Groer CE, Bohn LM. Functional selectivity at the μ-opioid receptor: implications for understanding opioid analgesia and tolerance. *Pharmacol Rev* 2011;**63**:1001−19.
11. Manglik A, Lin H, Aryal DK, McCorvy JD, Dengler D, Corder G, et al. Structure-based discovery of opioid analgesics with reduced side effects. *Nature* 2016;**537**:185−90.
12. Höllt V. Opioid peptide processing and receptor selectivity. *Annu Rev Pharmacol Toxicol* 1986;**26**:59−77.
13. Corder G, Castro DC, Bruchas MR, Scherrer G. Endogenous and exogenous opioids in pain. *Annu Rev Neurosci* 2018;**41**:453−73.
14. Horvath G. Endomorphin-1 and endomorphin-2: pharmacology of the selective endogenous μ-opioid receptor agonists. *Pharmacol Ther* 2000;**88**:437−63.
15. Latorraca NR, Venkatakrishnan AJ, Dror RO. GPCR dynamics: structures in motion. *Chem Rev* 2017;**117**:139−55.
16. Uprety R, Che T, Zaidi SA, Grinnell SG, Varga BR, Faouzi A, et al. Controlling opioid receptor functional selectivity by targeting distinct subpockets of the orthosteric site. *eLife* 2021;**10**:e56519.
17. Rosenbaum DM, Rasmussen SG, Kobilka BK. The structure and function of G-protein-coupled receptors. *Nature* 2009;**459**:356−63.
18. Granier S, Manglik A, Kruse AC, Kobilka TS, Thian FS, Weis WI, et al. Structure of the δ-opioid receptor bound to naltrindole. *Nature* 2012;**485**:400−4.
19. Wu H, Wacker D, Mileni M, Katritch V, Han GW, Vardy E, et al. Structure of the human κ-opioid receptor in complex with JDTic. *Nature* 2012;**485**:327−32.
20. Wang Y, Zhuang Y, DiBerto JF, Zhou XE, Schmitz GP, Yuan Q, et al. Structures of the entire human opioid receptor family. *Cell* 2023;**186**: 413−427.e17.
21. Portoghese PS. Bivalent ligands and the message−address concept in the design of selective opioid receptor antagonists. *Trends Pharmacol Sci* 1989;**10**:230−5.
22. Portoghese PS, Sultana M, Takemori AE. Design of peptidomimetic delta opioid receptor antagonists using the message−address concept. *J Med Chem* 1990;**33**:1714−20.
23. Shen Q, Qian Y, Huang X, Xu X, Li W, Liu J, et al. Discovery of potent and selective agonists of δ opioid receptor by revisiting the "message−address" concept. *ACS Med Chem Lett* 2016;**7**: 391−6.
24. Xiao L, Wang Y, Zhang M, Wu W, Kong L, Ma Y, et al. Discovery of a highly selective and potent κ opioid receptor agonist from *N*-cyclopropylmethyl-7α-phenyl-6,14-endoethanotetrahydronorthebaines with reduced central nervous system (CNS) side effects navigated by the message−address concept. *J Med Chem* 2019;**62**:11054−70.
25. Che T, Roth BL. Molecular basis of opioid receptor signaling. *Cell* 2023;**186**:5203−19.
26. Huang W, Manglik A, Venkatakrishnan AJ, Laeremans T, Feinberg EN, Sanborn AL, et al. Structural insights into μ-opioid receptor activation. *Nature* 2015;**524**:315−21.
27. Ballesteros JA, Weinstein H. Integrated methods for the construction of three-dimensional models and computational probing of structure−function relations in G protein-coupled receptors. *Methods in Neuroences* 1995;**25**:366−428.
28. Cheng JX, Cheng T, Li WH, Liu GX, Zhu WL, Tang Y. Computational insights into the subtype selectivity and "message−address−efficacy" mechanisms of opioid receptors through JDTic binding and unbinding. *Acta Pharmacol Sin* 2018;**39**:482−91.
29. Chang JK, Chang KJ. The role of amino-terminal sequence of beta-endorphin and dynorphin in the determination of opiate receptor type selectivity. *Life Sci* 1983;**33**(Suppl 1):267−9.
30. Chang KJ, Cuatrecasas P. Multiple opiate receptors. Enkephalins and morphine bind to receptors of different specificity. *J Biol Chem* 1979; **254**:2610−8.
31. Zadina JE, Hackler L, Ge LJ, Kastin AJ. A potent and selective endogenous agonist for the μ-opiate receptor. *Nature* 1997;**386**: 499−502.
32. Manglik A, Kruse AC, Kobilka TS, Thian FS, Mathiesen JM, Sunahara RK, et al. Crystal structure of the μ-opioid receptor bound to a morphinan antagonist. *Nature* 2012;**485**:321−6.
33. Manglik A. Molecular basis of opioid action: from structures to new leads. *Biol Psychiatry* 2020;**87**:6−14.
34. Yip KM, Fischer N, Paknia E, Chari A, Stark H. Atomic-resolution protein structure determination by cryo-EM. *Nature* 2020;**587**: 157−61.
35. Duan J, He XH, Li SJ, Xu HE. Cryo-electron microscopy for GPCR research and drug discovery in endocrinology and metabolism. *Nat Rev Endocrinol* 2024;**20**:349−65.
36. Katritch V, Cherezov V, Stevens RC. Structure−function of the G protein-coupled receptor superfamily. *Annu Rev Pharmacol Toxicol* 2013;**53**:531−56.
37. Limongelli V, Bonomi M, Marinelli L, Gervasio FL, Cavalli A, Novellino E, et al. Molecular basis of cyclooxygenase enzymes (COXs) selective inhibition. *Proc Natl Acad Sci U S A* 2010;**107**: 5411−6.
38. Dror RO, Pan AC, Arlow DH, Borhani DW, Maragakis P, Shan Y, et al. Pathway and mechanism of drug binding to G-protein-coupled receptors. *Proc Natl Acad Sci U S A* 2011;**108**:13118−23.
39. Reuveny E, Slesinger PA, Inglese J, Morales JM, Iñiguez-Lluhi JA, Lefkowitz RJ, et al. Activation of the cloned muscarinic potassium channel by G protein beta gamma subunits. *Nature* 1994;**370**:143−6.
40. Hill JJ, Peralta EG. Inhibition of a Gi-activated potassium channel (GIRK1/4) by the Gq-coupled m1 muscarinic acetylcholine receptor. *J Biol Chem* 2001;**276**:5505−10.
41. He C, Zhang H, Mirshahi T, Logothetis DE. Identification of a potassium channel site that interacts with G protein betagamma subunits to mediate agonist-induced signaling. *J Biol Chem* 1999;**274**: 12517−24.
42. Chan KW, Sui JL, Vivaudou M, Logothetis DE. Control of channel activity through a unique amino acid residue of a G protein-gated inwardly rectifying K+ channel subunit. *Proc Natl Acad Sci USA* 1996;**93**:14193−8.
43. Vivaudou M, Chan KW, Sui JL, Jan LY, Reuveny E, Logothetis DE. Probing the G-protein regulation of GIRK1 and GIRK4, the two subunits of the KACh channel, using functional homomeric mutants. *J Biol Chem* 1997;**272**:31553−60.
44. Yang D, Zhou Q, Labroska V, Qin S, Darbalaei S, Wu Y, et al. G protein-coupled receptors: structure- and function-based drug discovery. *Signal Transduct Targeted Ther* 2021;**6**:7.
45. Zhuang Y, Wang Y, He B, He X, Zhou XE, Guo S, et al. Molecular recognition of morphine and fentanyl by the human μ-opioid receptor. *Cell* 2022;**185**:4361−75.e19.
46. Dumitrascuta M, Bermudez M, Ben Haddou T, Guerrieri E, Schläfer L, Ritsch A, et al. *N*-Phenethyl substitution in 14-methoxy-*N*-methylmorphinan-6-ones turns selective μ opioid receptor ligands into dual μ/δ opioid receptor agonists. *Sci Rep* 2020;**10**:5653.
47. Zhang X, Sun MY, Zhang X, Guo CR, Lei YT, Wang WH, et al. Dynamic recognition of naloxone, morphine and endomorphin1 in the same pocket of μ-opioid receptors. *Front Mol Biosci* 2022;**9**: 925404.
48. Tömböly C, Ballet S, Feytens D, Kövér KE, Borics A, Lovas S, et al. Endomorphin-2 with a beta-turn backbone constraint retains the potent micro-opioid receptor agonist properties. *J Med Chem* 2008; **51**:173−7.
49. Eguchi M, Shen RY, Shea JP, Lee MS, Kahn M. Design, synthesis, and evaluation of opioid analogues with non-peptidic beta-turn

scaffold: Enkephalin and endomorphin mimetics. *J Med Chem* 2002; **45**:1395−8.
50. Jerabek-Willemsen M, André T, Wanner R, Roth HM, Duhr S, Baaske P, et al. MicroScale thermophoresis: interaction analysis and beyond. *J Mol Struct* 2014;**1077**:101−13.
51. Guo CR, Zhang ZZ, Zhou X, Sun MY, Li TT, Lei YT, et al. Chronic cough relief by allosteric modulation of P2X3 without taste disturbance. *Nat Commun* 2023;**14**:5844.
52. Zhao WS, Wang J, Ma XJ, Yang Y, Liu Y, Huang LD, et al. Relative motions between left flipper and dorsal fin domains favour P2X4 receptor activation. *Nat Commun* 2014;**5**:4189.
53. Jiang R, Taly A, Lemoine D, Martz A, Cunrath O, Grutter T. Tightening of the ATP-binding sites induces the opening of P2X receptor channels. *EMBO J* 2012;**31**:2134−43.
54. Alberts IL, Nadassy K, Wodak SJ. Analysis of zinc binding sites in protein crystal structures. *Protein Sci* 1998;**7**:1700−16.
55. Yang F, Xiao X, Lee BH, Vu S, Yang W, Yarov-Yarovoy V, et al. The conformational wave in capsaicin activation of transient receptor potential vanilloid 1 ion channel. *Nat Commun* 2018;**9**:2879.
56. Chatterjee A, Guo J, Lee HS, Schultz PG. A genetically encoded fluorescent probe in mammalian cells. *J Am Chem Soc* 2013;**135**: 12540−3.
57. Lester HA, Karschin A. Gain of function mutants: ion channels and G protein-coupled receptors. *Annu Rev Neurosci* 2000;**23**:89−125.
58. Magalhaes AC, Dunn H, Ferguson SS. Regulation of GPCR activity, trafficking and localization by GPCR-interacting proteins. *Br J Pharmacol* 2012;**165**:1717−36.
59. Wickström SA, Fässler R. Regulation of membrane traffic by integrin signaling. *Trends Cell Biol* 2011;**21**:266−73.
60. Tottene A, Fellin T, Pagnutti S, Luvisetto S, Striessnig J, Fletcher C, et al. Familial hemiplegic migraine mutations increase Ca^{2+} influx through single human CaV2.1 channels and decrease maximal CaV2.1 current density in neurons. *Proc Natl Acad Sci U S A* 2002; **99**:13284−9.
61. Berecki G, Tao E, Howell KB, Coorg RK, Andersen E, Kahlig K, et al. Nav1.2 channel mutations preventing fast inactivation lead to SCN2A encephalopathy. *Brain* 2025;**148**:212−26.
62. Zhang HL, Hu BX, Li ZL, Du T, Shan JL, Ye ZP, et al. PKCβII phosphorylates ACSL4 to amplify lipid peroxidation to induce ferroptosis. *Nat Cell Biol* 2022;**24**:88−98.
63. Zhang Y, Sun L, Xuan L, Pan Z, Hu X, Liu H, et al. Long non-coding RNA CCRR controls cardiac conduction *via* regulating intercellular coupling. *Nat Commun* 2018;**9**:4176.
64. Chavkin C, Goldstein A. Specific receptor for the opioid peptide dynorphin: structure−activity relationships. *Proc Natl Acad Sci U S A* 1981;**78**:6543−7.
65. Schwyzer R. ACTH: a short introductory review. *Ann N Y Acad Sci* 1977;**297**:3−26.
66. Stank A, Kokh DB, Fuller JC, Wade RC. Protein binding pocket dynamics. *Acc Chem Res* 2016;**49**:809−15.
67. Mansour A, Taylor LP, Fine JL, Thompson RC, Hoversten MT, Mosberg HI, et al. Key residues defining the μ-opioid receptor binding pocket: a site-directed mutagenesis study. *J Neurochem* 1997;**68**:344−53.
68. Xu X, Kaindl J, Clark MJ, Hübner H, Hirata K, Sunahara RK, et al. Binding pathway determines norepinephrine selectivity for the human β_1AR over β_2AR. *Cell Res* 2021;**31**:569−79.
69. Feng Y, He X, Yang Y, Chao D, Lazarus LH, Xia Y. Current research on opioid receptor function. *Curr Drug Targets* 2012;**13**:230−46.
70. Fricker LD, Margolis EB, Gomes I, Devi LA. Five decades of research on opioidpeptides: current knowledge and unanswered questions. *Mol Pharmacol* 2020;**98**:96−108.
71. Chavkin C, James IF, Goldstein A. Dynorphin is a specific endogenous ligand of the kappa opioid receptor. *Science* 1982;**215**: 413−5.
72. Meunier JC, Mollereau C, Toll L, Suaudeau C, Moisand C, Alvinerie P, et al. Isolation and structure of the endogenous agonist of opioid receptor-like ORL1 receptor. *Nature* 1995;**377**:532−5.
73. James IF, Chavkin C, Goldstein A. Preparation of brain membranes containing a single type of opioid receptor highly selective for dynorphin. *Proc Natl Acad Sci U S A* 1982;**79**:7570−4.
74. Onogi T, Minami M, Katao Y, Nakagawa T, Aoki Y, Toya T, et al. DAMGO, a mu-opioid receptor selective agonist, distinguishes between mu- and delta-opioid receptors around their first extracellular loops. *FEBS Lett* 1995;**357**:93−7.
75. Lazarus LH, Bryant SD, Salvadori S, Attila M, Sargent Jones L. Opioid infidelity: novel opioid peptides with dual high affinity for delta- and mu-receptors. *Trends Neurosci* 1996;**19**:31−5.
76. Koehl A, Hu H, Maeda S, Zhang Y, Qu Q, Paggi JM, et al. Structure of the μ-opioid receptor−G_i protein complex. *Nature* 2018;**558**:547−52.
77. Siuda ER, Carr R, Rominger DH, Violin JD. Biased mu-opioid receptor ligands: a promising new generation of pain therapeutics. *Curr Opin Pharmacol* 2017;**32**:77−84.
78. Rehrauer KJ, Cunningham CW. Bivalent and bifunctional opioid receptor ligands as novel analgesics. *Pharmacol Res* 2023;**197**:106966.
79. Kalso E. Oxycodone. *J Pain Symptom Manag* 2005;**29**:S47−56.
80. Ye RR, Jiang S, Xu X, Lu Y, Wang YJ, Liu JG. Dezocine as a potent analgesic: overview of its pharmacological characterization. *Acta Pharmacol Sin* 2022;**43**:1646−57.
81. Goudra B. Oliceridine-Opioid of the 21st century. *Saudi J Anaesth* 2022;**16**:69−75.
82. Dhillon S. Tegileridine: first approval. *Drugs* 2024;**84**:717−20.
83. DeWire SM, Yamashita DS, Rominger DH, Liu G, Cowan CL, Graczyk TM, et al. A G protein-biased ligand at the μ-opioid receptor is potently analgesic with reduced gastrointestinal and respiratory dysfunction compared with morphine. *J Pharmacol Exp Therapeut* 2013;**344**:708−17.
84. Huang YZ, Ma JX, Bian YJ, Bai QR, Gao YH, Di SK, et al. TRPV1 analgesics disturb core body temperature *via* a biased allosteric mechanism involving conformations distinct from that for nociception. *Neuron* 2024;**112**:1815−31.e4.
85. Sun MY, Zhang X, Yu PC, Liu D, Yang Y, Cui WW, et al. Vanilloid agonist-mediated activation of TRPV1 channels requires coordinated movement of the S1−S4 bundle rather than a quiescent state. *Sci Bull (Beijing)* 2022;**67**:1062−76.
86. Rascol E, Dufourquet A, Baccouch R, Soule P, Alves ID. An original approach to measure ligand/receptor binding affinity in non-purified samples. *Sci Rep* 2022;**12**:5400.
87. Casarotto PC, Girych M, Fred SM, Kovaleva V, Moliner R, Enkavi G, et al. Antidepressant drugs act by directly binding to TRKB neurotrophin receptors. *Cell* 2021;**184**:1299−313.e19.
88. Chovancova E, Pavelka A, Benes P, Strnad O, Brezovsky J, Kozlikova B, et al. C 3.0: a tool for the analysis of transport pathways in dynamic protein structures. *PLoS Comput Biol* 2012;**8**:e1002708.
89. Najibi SM, Maadooliat M, Zhou L, Huang JZ, Gao X. Protein structure classification and loop modeling using multiple ramachandran distributions. *Comput Struct Biotechnol J* 2017;**15**:243−54.
90. Pal S, Sengupta K. Computational-based insights into the phylogeny, structure, and function of Rhodococcus alkane-1-monooxygenase. *3 Biotech* 2020;**10**:391.
91. Dror RO, Arlow DH, Maragakis P, Mildorf TJ, Pan AC, Xu H, et al. Activation mechanism of the β2-adrenergic receptor. *Proc Natl Acad Sci U S A* 2011;**108**:18684−9.
92. Lomize MA, Pogozheva ID, Joo H, Mosberg HI, Lomize AL. OPM database and PPM web server: resources for positioning of proteins in membranes. *Nucleic Acids Res* 2012;**40**:D370−6.
93. *Schrödinger release 2018-1: desmond molecular dynamics system, D. E. Shaw research*. 2018. New York, NY.
94. George A, Kaminski RA. Friesner. Evaluation and reparametrization of the OPLS-AA force field for proteins *via* comparison with accurate quantum chemical calculations on peptides. *J Phys Chem B* 2001;**105**:6474−87.
95. William L, Jorgensen SD, Maxwell, Tirado-Rives J. Development and testing of the OPLS all-atom force field on conformational energetics and properties of organic liquids. *J Am Chem Soc* 1996;**118**: 11225−36.

96. Banks JL, Beard HS, Cao Y, Cho AE, Damm W, Farid R, et al. Integrated modeling program, applied chemical theory (IMPACT). *J Comput Chem* 2005;**26**:1752−80.
97. *Schrödinger release 2018-1*. New York, NY: Maestro, Schrödinger, LLC; 2023.
98. Clark AJ, Tiwary P, Borrelli K, Feng S, Miller EB, Abel R, et al. Prediction of protein−ligand binding poses *via* a combination of induced fit docking and metadynamics simulations. *J Chem Theory Comput* 2016;**12**:2990−8.
99. Xu J, Cao XM, Hu P. Accelerating metadynamics-based free-energy calculations with adaptive machine learning potentials. *J Chem Theory Comput* 2021;**17**:4465−76.
100. Gervasio FL, Laio A, Parrinello M. Flexible docking in solution using metadynamics. *J Am Chem Soc* 2005;**127**:2600−7.